B^0-$\bar{B}^0$ mixing and $B \to X_s\gamma$ decay in the third type 2HDM: Effects of NLO QCD contributions

Zhenjun Xiao*
Department of Physics, Nanjing Normal University, Nanjing, Jiangsu 210097, People's Republic of China and High Energy Section, ICTP, Strada Costiera 11, 34014 Trieste, Italy

Libo Guo†
Department of Physics, Nanjing Normal University, Nanjing, Jiangsu 210097, People's Republic of China
(Received 12 September 2003; published 9 January 2004)

In this paper, we calculate the next-to-leading order (NLO) new physics contributions to the mass splitting ΔM_{B_d} and the branching ratio $\mathcal{B}(B\to X_s\gamma)$ induced by the charged Higgs loop diagrams in the third type of two-Higgs-doublet models (model III) and draw the constraints on the free parameters of model III. For the model III under consideration, we find that (a) an upper limit $|\lambda_{tt}|\leqslant 1.7$ is obtained from the precision data of $\Delta M_{B_d}=0.502\pm 0.007\ \mathrm{ps}^{-1}$, while $|\lambda_{tt}|\approx 0.5$ is favored phenomenologicaly, (b) for $B\to X_s\gamma$ decay, the NLO QCD contributions tend to cancel the LO new physics contributions, (c) a light charged Higgs boson with a mass around or even less than 200 GeV is still allowed at the NLO level by the measured branching ratio $\mathcal{B}(B\to X_s\gamma)$, numerically, $188\leqslant M_H\leqslant 215$ GeV for $(|\lambda_{tt}|,|\lambda_{bb}|)=(0.5,18)$, (d) the NLO QCD contributions tend to cancel the LO contributions effectively, the lower limit on M_H being consequently decreased by about 200 GeV, and (e) the allowed region of M_H will be shifted toward the heavy mass end for a nonzero relative phase θ between the Yukawa couplings λ_{tt} and λ_{bb}. The numerical results for the conventional model II are also presented for the sake of comparison.

DOI: 10.1103/PhysRevD.69.014002 PACS number(s): 13.20.He, 12.60.Fr, 14.40.Nd

I. INTRODUCTION

Among the physical observables of B meson mixing and decays, the mass splitting ΔM_{B_d} and the branching ratio $\mathcal{B}(B\to X_s\gamma)$ have been measured with high precision. The recent world averages as given in Refs. [1–3] are

$$\mathcal{B}(B\to X_s\gamma)=(3.34\pm 0.38)\times 10^{-4}, \tag{1}$$

$$\Delta M_{B_d}=0.502\pm 0.007\ \ \mathrm{ps}^{-1}, \tag{2}$$

which are in perfect agreement with the next-to-leading order standard model (SM) predictions, for example, presented in Refs. [4] and [5]. Obviously, there is only a little room left for new physics effects beyond the SM. By comparing the theoretical predictions with the precision data, strong constraints on the parameter space of new physics models can be obtained.

During the past decade, the $B\to X_s\gamma$ decay has been studied in great detail in the SM and various new physics models. At present, the complete next-to-leading order (NLO) calculations of this decay mode are available for the SM [6–11], for the conventional two-Higgs-doublet models (2HDM) [4,9,12,13], for some supersymmetric models [14,15], and for left-right symmetric models [15]. The studies at leading order (LO) for model III [16–19], for the top-two-Higgs-doublet model [20], and the technicolor models [21] are also available. From relevant theoretical calculations, we know that the rare decay $B\to X_s\gamma$ is very sensitive to the new physics contributions and has been used as the first test for new physics models.

In Ref. [4], Borzumati and Greub studied the $B\to X_s\gamma$ decay in NLO QCD in a class of models containing at least two Higgs doublets, with only one charged Higgs boson non-decoupled at low energy, and found the constraints on the mass of charged Higgs boson for model II: the popular type-II two-Higgs-doublet model. In this paper, we will extend their work [4] to the case of model III (the third type two-Higgs-doublet model [22]), to constrain the charged Higgs boson mass M_H, as well as the Yuakawa couplings λ_{tt} and λ_{bb} after the inclusion of the NLO QCD corrections.

The strength of the B_d^0-$\bar{B}_d^0$ mixing is described by the mass splitting ΔM_{B_d}. In the SM, ΔM_{B_d} is strongly dominated by the box diagrams involving the heavy top quark and W gauge boson. In new physics models, the box diagrams where one or two W gauge bosons are replaced by other charged particles can also contribute to this quantity. The well measured ΔM_{B_d} therefore can be used to constrain the new physics models.

In Ref. [5], the authors presented a calculation of the mass splitting ΔM_{B_d} at the NLO level in the conventional model II and found that the NLO corrections enhance the LO results by about 18%. In Ref. [18], the LO new physics contributions to ΔM_{B_d} have been calculated in model III and the constraint on the Yukawa coupling λ_{tt} was also given by neglecting the large uncertainty of the nonperturbative parameter $f_{B_d}\sqrt{\hat{B}_{B_d}}$. We here will calculate the charged Higgs contribution to mass splitting ΔM_{B_d} at the NLO level in the

*Electronic address: xiaozhenjun@pine.njnu.edu.cn
†Electronic address: guolb@email.njnu.edu.cn

model III, use the new high precision data to constrain $|V_{td}|$ and $|\lambda_{tt}|$ and consider the effects of the large uncertainty of $f_{B_d}\sqrt{\hat{B}_{B_d}}$.

This paper is organized as follows. In Sec. II, we describe the basic structures of model III, and give a brief review about the known constraints on model III presented in previous works. In Sec. III, we calculate the mass splitting ΔM_{B_d} at the NLO level in model III and draw the constraint on $|\lambda_{tt}|$ by employing the new precision data. In Sec. IV, the NLO new physics contributions to the branching ratio $\mathcal{B}(B\to X_s\gamma)$ in model III are calculated and analyzed in great detail. The numerical results for the conventional model II at the NLO level are also presented as a comparison. The conclusions are included in the final section.

II. STRUCTURE OF MODEL III AND CONSTRAINT

The simplest extension of the SM is the so-called two-Higgs-doublet models [23,24]. In such models, the tree level flavor-changing neutral currents (FCNCs) are absent if one introduces an *ad hoc* discrete symmetry to constrain the 2HDM scalar potential and Yukawa Lagrangian. Let us consider a Yukawa Lagrangian of the form [17]

$$\mathcal{L}_Y=\eta^U_{ij}\overline{Q}_{i,L}\widetilde{\phi_1}U_{j,R}+\eta^D_{ij}\overline{Q}_{i,L}\phi_1 D_{j,R}+\xi^U_{ij}\overline{Q}_{i,L}\widetilde{\phi_2}U_{j,R}+\xi^D_{ij}\overline{Q}_{i,L}\phi_2 D_{j,R}+\text{H.c.}, \tag{3}$$

where ϕ_i $(i=1,2)$ are the two Higgs doublets, $\tilde{\phi}_{1,2}=i\tau_2\phi^*_{1,2}$, $Q_{i,L}$ $(U_{j,R})$ with $i=(1,2,3)$ are the left-handed isodoublet quarks (right-handed up-type quarks), $D_{j,R}$ are the right-handed isosinglet down-type quarks, while $\eta^{U,D}_{i,j}$ and $\xi^{U,D}_{i,j}$ $(i,j=1,2,3$ are the family indices) are generally the nondiagonal matrices of the Yukawa coupling. By imposing the discrete symmetry

$$\phi_1\to-\phi_1,\quad \phi_2\to\phi_2,\quad D_i\to-D_i,\quad U_i\to\mp U_i \tag{4}$$

one obtains the so called model I and model II. In model I the third and fourth terms in Eq. (3) will be dropped by the discrete symmetry; therefore, both the up- and down-type quarks get mass from Yukawa couplings to the same Higgs doublet ϕ_1, while the ϕ_2 has no Yukawa couplings to the quarks. For model II, on the other hand, the first and fourth terms in Eq. (3) will be dropped by imposing the discrete symmetry. Model II has, consequently, the up- and down-type quarks getting mass from Yukawa couplings to two different scalar doublets ϕ_1 and ϕ_2.

During the past years, models I and II have been studied extensively in literature at LO [26] and NLO levels [4,9,12,13] and tested experimentally. Model II has been very popular since it is the building block of the minimal supersymmetric standard model. In this paper, we focus on the third type of 2HDM [22], usually known as model III [17,22]. In model III, no discrete symmetry is imposed and both up- and down-type quarks then may have diagonal and/or flavor-changing couplings with ϕ_1 and ϕ_2. As described in Ref. [17], one can choose a suitable basis $(H^0,H^1,H^2,H^\pm)$ to express two Higgs doublets [17],

$$\phi_1=\frac{1}{\sqrt{2}}\begin{pmatrix}\sqrt{2}\chi^+\\ v+H^0+i\chi^0\end{pmatrix},\quad \phi_2=\frac{1}{\sqrt{2}}\begin{pmatrix}\sqrt{2}H^+\\ H^1+iH^2\end{pmatrix}, \tag{5}$$

and take their vacuum expectation values as the form

$$\langle\phi_1\rangle=\begin{pmatrix}0\\ v/\sqrt{2}\end{pmatrix},\quad \langle\phi_2\rangle=0, \tag{6}$$

where $v=(\sqrt{2}G_F)^{-1/2}=246$ GeV. The transformation relation between (H^0,H^1,H^2) and the mass eigenstates $(\bar{H}^0,h^0,A^0)$ can be found in Ref. [17]. The $H^\pm$ are the physical charged Higgs bosons, H^0 and h^0 are the physical *CP*-even neutral Higgs bosons and the A^0 is the physical CP-odd neutral Higgs boson. After the rotation of quark fields, the Yukawa Lagrangian of quarks are of the form [17],

$$\mathcal{L}^{\rm III}_Y=\eta^U_{ij}\overline{Q}_{i,L}\widetilde{\phi_1}U_{j,R}+\eta^D_{ij}\overline{Q}_{i,L}\phi_1 D_{j,R}+\hat{\xi}^U_{ij}\overline{Q}_{i,L}\widetilde{\phi_2}U_{j,R}+\hat{\xi}^D_{ij}\overline{Q}_{i,L}\phi_2 D_{j,R}+\text{H.c.}, \tag{7}$$

where $\eta^{U,D}_{ij}$ correspond to the diagonal mass matrices of up- and down-type quarks, while the neutral and charged flavor-changing couplings[1] will be [17]

$$\hat{\xi}^{U,D}_{neutral}=\xi^{U,D},\quad \hat{\xi}^U_{charged}=\xi^U V_{CKM},\quad \hat{\xi}^D_{charged}=V_{CKM}\xi^D, \tag{8}$$

with

$$\xi^{U,D}_{ij}=\frac{g\sqrt{m_i m_j}}{\sqrt{2}M_W}\lambda_{ij}, \tag{9}$$

where V_{CKM} is the Cabibbo-Kobayashi-Maskawa mixing matrix [25], $i,j=(1,2,3)$ are the generation indices. It is easy to see from Eq. (9) that the FCNC within the first two generations are naturally suppressed by the small quark masses, while a larger freedom in still allowed for the FCNC involving the top and bottom quarks. The coupling constants λ_{ij} are free parameters to be determined by experiments, and they may also be complex.

In the conventional model I and model II, the only additional contribution to the $B\to X_s\gamma$ decay with respect to the SM comes from the charged Higgs boson–top quark penguin diagrams and depends on the mass of the charged Higgs boson, $M_{H^\pm}$, and on $\tan\beta=v_2/v_1$, where $v_{1,2}$ are the vacuum expectation values of $\phi_{1,2}$. From currently available studies at the NLO level [4,9,12,13], one get to know the following main features of model II:

(a) The charged Higgs penguins interfere constructively with their SM counterparts, and thus always enhance the branching ratio $\mathcal{B}(B\to X_s\gamma)$. The excellent agreement between theory and experiments for the decay rate therefore leads to a strong lower bound on the mass $M_{H^\pm}$. One typical lower bound (99% C.L.) at NLO level as given in Ref. [9] is

[1]We make the same ansatz on the $\xi^{U,D}_{ij}$ couplings as in Ref. [17]. For more details about the definition of $\hat{\xi}^{U,D}$, see Ref. [17].

$$M_{H^\pm} > 315 \text{ GeV} \tag{10}$$

for any value of $\tan\beta$.

(b) The inclusion of NLO corrections shift the lower bound up by about 30% [12]. In other words, the lower bound on $M_{H^\pm}$ will become stronger in the NLO level than that in the LO level. One lower bound as given in Ref. [12] is $M_{H^\pm} > 258$ GeV using the LO calculation, but $M_{H^\pm} > 368$ GeV using the NLO calculation.

(c) The lower bound on $M_{H^\pm}$ from the measured branching ratio $\mathcal{B}(B\to X_s\gamma)$ depends very sensitively on small effects, and in particular on the way various errors are combined. The difference is usually about 100 GeV or even larger [12]. Since the theoretical error is significantly reduced at the NLO level, improving the calculation to the NLO has important effects on the lower bounds on $M_{H^\pm}$.

(d) The bound on $M_{H^\pm}$ from the $B\to X_s\gamma$ decay is much stronger than those from other experiments. As shown in Fig. 4 of Ref. [9], for example, the direct limit from LEP experiments is only $M_{H^\pm} > 78.6$ GeV [2], the ratio $R_b = \Gamma(Z\to b\bar{b})/\Gamma(Z\to \text{hadrons})$ is relevant only for very small $\tan\beta$, while rare $B\to\tau$ decays constrain $M_{H^\pm}$ only for large $\tan\beta$.

(e) The $\tan\beta$ dependence of the lower bound saturates for $\tan\beta \gtrsim 5$.

For model I, however, no bound on $M_{H^\pm}$ can be obtained from $B\to X_s\gamma$ [27], since the charged Higgs loops interfere destructively with the SM penguin diagrams and decouple for large $\tan\beta$.

Although many phenomenological investigations have been done in the framework of model III [16–19,22,28,29], the situation here is still not as clear as in model II, since there are many more free parameters in model III than in model II. As pointed in Ref. [17], the data of K^0-$\bar{K}^0$ and B_d^0-$\bar{B}_d^0$ mixing processes put severe constraint on the flavor-changing couplings involving the first generation of quarks. It is therefore reasonable to assume that the Yukawa couplings involving the u and d quarks are zero: $\lambda_{uj} = \lambda_{dj} = 0$ for $j = 1,2,3$.

In Ref. [18], Chao *et al.* studied the decay $b\to s\gamma$ at the leading order by assuming that only the couplings λ_{tt} and λ_{bb} are nonzero. They found that the constraint on $M_{H^\pm}$ imposed by the CLEO data of $b\to s\gamma$ can be greatly relaxed by considering the phase effects of λ_{tt} and λ_{bb}. The constraints from B^0-$\bar{B}^0$ mixing, the neutron electric dipole moment (NEDM), the Z^0-pole parameter ρ, and R_b were also considered in Ref. [18]. The Chao-Cheung-Keung (CCK) scenario of model III [18] has the following advantages:

(i) Since one keeps only the couplings λ_{tt} and λ_{bb} that are not zero, the neutral Higgs bosons do not contribute at tree level or one-loop level. The new contributions therefore come only from the charged Higgs loop diagrams with the heavy internal top quark.

(ii) The new operators $O_{9,10}$ and all flipped chirality partners of operators $O_{1,\ldots,10}$ as defined in Ref. [28] do not contribute to the decay $b\to s\gamma$.

The free parameters in model III are greatly reduced to λ_{tt}, λ_{bb}, and $M_{H^\pm}$.

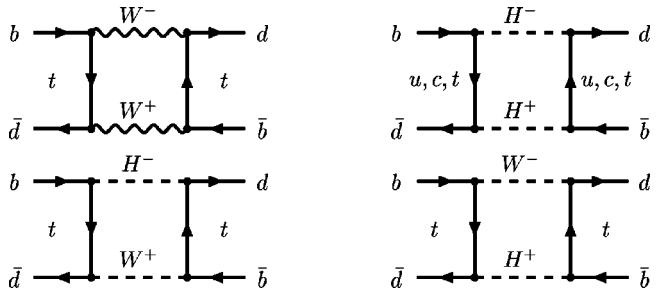

FIG. 1. The box diagrams for the B_d^0-$\bar{B}_d^0$ mixing in the framework of the 2HDM at the lowest order. More crossed diagrams are not shown. For those Feynman diagrams of NLO QCD corrections obtained by connecting any two quark lines with a gluon line, see the figures in Ref. [5].

In the following sections, we will calculate the NLO QCD contributions to the mass splitting ΔM_{B_d} and the branching ratio $\mathcal{B}(B\to X_s\gamma)$, to find the constraints on the parameters λ_{tt}, λ_{bb}, and M_H of model III. We will study the effects of the NLO QCD contributions in detail, and will also compare the results in model III with those in model II.

III. B^0-$\bar{B}^0$ MIXING IN MODEL III

B^0-$\bar{B}^0$ mixing is in general a FCNC process generated through weak interactions. At the lowest order of perturbation theory and in model III, the corresponding box diagrams that generate this process are shown in Fig. 1. The charged-Higgs boson contributions to B^0-$\bar{B}^0$ mixing at leading order were calculated some time ago [30]. The NLO QCD corrections to B^0-$\bar{B}^0$ mixing was first presented in Ref. [31] for the SM, and in Ref. [5] for the conventional 2HDM: model I and model II. The possible constraints on model III from the measured parameter $x_d = \Delta M_B/\Gamma_B$ were studied, for example, in Refs. [17,18,32] at the LO level.

A. The basic formulas

The strengths of the B_q^0-$\bar{B}_q^0$ mixing with $q \in (d,s)$ are described by the mass differences $\Delta M_{B_q} = M_H^q - M_L^q$ where the subscripts H and L denote the heavy and light mass eigenstates, respectively. The long distance contributions are estimated to be very small. The top-box diagram is strongly dominant, while the charm and mixed top-charm contributions are entirely negligible.

Recently, great progress have been made in experimental measurements. For ΔM_{B_s}, a lower limit of $\Delta M_{B_s} > 14.1\ \text{ps}^{-1}$ at 95% C.L. is available. For ΔM_{B_d}, however, it has been measured with high precision: the world average [2,3] is $\Delta M_{B_d} = 0.502 \pm 0.007$ and dominated by the results of B factories. At the end of the LEP-CDF-SLD era, ΔM_{B_d} had been measured with a relative precision of about 2.6% [33]. After including the B factory measurements, the precision is now 1.2% and high enough to constrain the new physics contributions effectively.

On the theoretical side, the NLO theoretical prediction of ΔM_{B_d} is available now in the SM and in some new physics models beyond. In SM the mass difference ΔM_{B_d} can be written as [34]

$$\Delta M_{B_d} = \frac{G_F^2}{6\pi^2} m_B |V_{td}|^2 (\hat{B}_{B_d} f_{B_d}^2) M_W^2 \eta_B S_0(x_t), \quad (11)$$

with

$$S_0(x) = \frac{4x - 11x^2 + x^3}{4(1-x)^2} - \frac{3x^3}{2(1-x)^3} \ln[x], \quad (12)$$

$$\hat{B}_{B_d} = B_{B_d}(\mu)[\alpha_s^{(5)}(\mu)]^{-6/23}\left[1 + \frac{\alpha_s^{(5)}(\mu)}{4\pi} J_5\right], \quad (13)$$

$$\eta_B = [\alpha_S(\mu_t)]^{6/23}\left[1 + \frac{\alpha_S(\mu_t)}{4\pi}\left(\frac{S_1(x_t)}{S_0(x_t)} + B_t - J_5 + \frac{\gamma^{(0)}}{2}\ln\frac{\mu_t^2}{M_W^2} + \gamma_{m0}\frac{\partial \ln S_0(x_t)}{\partial \ln x_t}\ln\frac{\mu_t^2}{M_W^2}\right)\right], \quad (14)$$

where $x_t = \overline{m}_t(\mu_t)/M_W^2$,[2] $\gamma^{(0)} = 4$, and $\gamma_{m0} = 8$ for $SU(3)_C$, $B_t = 17/3$ and $J_5 = 5165/3174$ in the NDR scheme [34], $m_B = 5.279$ GeV [2] is B_d^0 meson mass, $\eta_B = 0.55 \pm 0.01$ summarizes the NLO QCD corrections [5,31], the function $S_0(x_t)$ describes the dominant top-box contribution, f_{B_d} is the B_d^0 meson decay constant, and $\hat{B}$ is the renormalization group invariant and nonperturbative parameter. There are many works that estimate the values of f_{B_d} and $\hat{B}_{B_d}$ in lattice QCD calculation and in QCD sum rules [33]. The definitions of the various quantities in Eq. (14) can be found, for example, in Ref. [34]. Using the input parameters as given in Appendix A, we find numerically that $\eta_B = 0.553$ and 0.496 for $\mu_t = 170$ GeV or $\mu_t = M_W$, respectively. The product $\eta_B S_0(x_t)$ has, however, a very weak dependence on μ_t at the NLO level: the uncertainty is only 0.3% for 100 GeV$\leqslant \mu_t \leqslant$300 GeV.

With a well measured ΔM_{B_d}, one can determine $|V_{td}|$ from Eq. (11) in the framework of the SM. Using the input parameters as given in Appendix A, we find a limit on $|V_{td}|$ from the measured ΔM_{B_d} in Eq. (11):

$$|V_{td}| = [7.9 \pm 1.6(f_{B_d}\sqrt{\hat{B}_{B_d}}) \pm 0.2(m_t) \pm 0.1(\eta_B)] \times 10^{-3} = (7.9 \pm 1.7) \times 10^{-3}, \quad (15)$$

where the uncertainties of $f_{B_d}\sqrt{\hat{B}_{B_d}}$, m_t, and η_B as listed in Appendix A have been considered and added in quadrature.

[2] $\overline{m}_q(\mu)$ is the running q-quark mass in the modified minimal subtraction ($\overline{\text{MS}}$) scheme at the renormalization scale μ. For details, see Appendix A.

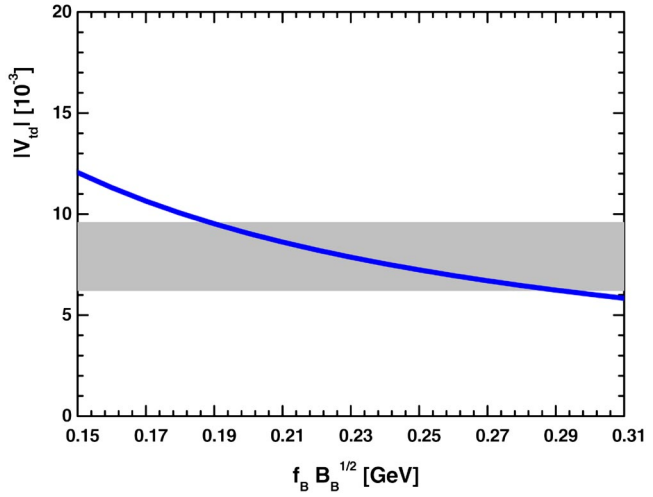

FIG. 2. Contour plot of $|V_{td}|$ vs the nonperturbative parameter $f_{B_d}\sqrt{\hat{B}_{B_d}}$ by using the well measured mass splitting $\Delta M_{B_d} = 0.502 \pm 0.007$ ps^{-1}. The shaded band corresponds to the limit $|V_{td}| = (7.9 \pm 1.7) \times 10^{-3}$ obtained from the measured ΔM_{B_d}. The width of the curve shows the effect of uncertainties of other quantities in Eq. (11).

In the following calculations, we will use this value of $|V_{td}|$ as input. It is easy to see that the error of $|V_{td}|$ is almost completely determined by the uncertainty of the factor $f_{B_d}\sqrt{\hat{B}_{B_d}}$. If this uncertainty can be decreased by a factor of 2, we would find

$$|V_{td}| = (7.9 \pm 1.1) \times 10^{-3}. \quad (16)$$

Figure 2 is the contour plot in $f_{B_d}\sqrt{\hat{B}_{B_d}}$-$|V_{td}|$ plane obtained by the using the data $\Delta M_{B_d} = 0.502 \pm 0.007$ ps^{-1}. The shaded band in Fig. 2 shows the allowed region as given in Eq. (15). The solid line shows the $f_{B_d}\sqrt{\hat{B}_{B_d}}$ dependence of $|V_{td}|$ and the width of the line shows the effect of uncertainties of all other quantities appearing in Eq. (11).

B. Mass splitting ΔM_{B_d} in models II and III

In the two-Higgs-doublet models, the charged Higgs boson contributes to the mass splitting ΔM_{B_d}. In Ref. [18], the authors calculated the new physics contribution to ΔM_{B_d} in model III at the leading order and presented the constraint on the λ_{tt}-M_H plane by using the measured $x_d = \Delta M_{B_d}/\Gamma_B$. But they did not consider the effects of the large uncertainty of nonperturbative parameter $f_{B_d}\sqrt{\hat{B}_{B_d}}$ and the new physics contribution to the parameter η_B.

Since ΔM_{B_d} has been measured with very high precision, we use this quantity directly instead of the parameter x_d in our calculation. We will calculate the charged Higgs contribution to mass splitting ΔM_{B_d} at the NLO level by extending the work in Ref. [5] to the case of model III. We will consider the effects of the large uncertainty of $f_{B_d}\sqrt{\hat{B}_{B_d}}$.

In the framework of 2HDM, the NLO mass difference ΔM_{B_d} can be written as [5]

$$\Delta M_{B_d}=\frac{G_F^2}{6\pi^2}m_B M_W^2|V_{td}|^2(\hat{B}_{B_d}f_{B_d}^2)\,\eta_B(x_t,y_t)S_{2HDM}(x_t,y_t), \tag{17}$$

with

$$\eta_B(x_t,y_t)=\alpha_S(M_W)^{6/23}\times\left[1+\frac{\alpha_S(M_W)}{4\pi}\left(\frac{D_{2HDM}(x_t,y_t)}{S_{2HDM}(x_t,y_t)}-J_5\right)\right] \tag{18}$$

and

$$S_{2HDM}(x_t,y_t)=[S_0(x_t)+S_{WH}(x_t,y_t)+S_{HH}(x_t,y_t)], \tag{19}$$

$$D_{2HDM}=D_{SM}(x_t)+D_H(x_t,y_t), \tag{20}$$

where $x_t=\bar{m}_t^2(M_W)/M_W^2$ and $y_t=\bar{m}_t^2(M_W)/M_H^2$, and the high energy matching scale has been chosen as $\mu=M_W$. The functions $D_{SM}(x_t)$ and $D_H(x_t,y_t)$ in Eq. (20) describe the SM and new physics part of the NLO QCD corrections to the mass splitting ΔM_{B_d} [5],

$$D_{SM}(x_t)=C_F[L^{(1,SM)}(x_t)+3S_0(x_t)]+C_A[L^{(8,SM)}(x_t)+5S_0(x_t)], \tag{21}$$

$$D_H(x_t,y_t)=C_F\{L^{(1,H)}(x_t,y_t)+3[S_{WH}(x_t,y_t)+S_{HH}(x_t,y_t)]\}+C_A\{L^{(8,H)}(x_t,y_t)+5[S_{WH}(x_t,y_t)+S_{HH}(x_t,y_t)]\}, \tag{22}$$

where $C_F=4/3$ and $C_A=1/3$ for $SU(3)_C$. The function $S_0(x_t)$ describes the dominant top-box contribution in the SM and has been given in Eq. (12). The functions $S_{WH}(x_t,y_t)$ and $S_{HH}(x_t,y_t)$ denote the new physics contributions from the box diagrams with one or two charged Higgs involved [5],

$$S_{WH}(x_t,y_t)=|Y|^2\frac{y_t x_t}{4}\left[\frac{(2x_t-8y_t)\ln(y_t)}{(1-y_t)^2(y_t-x_t)}+\frac{6x_t\ln(x_t)}{(1-x_t)^2(y_t-x_t)}-\frac{8-2x_t}{(1-y_t)(1-x_t)}\right], \tag{23}$$

$$S_{HH}(y_t)=|Y|^4\frac{y_t x_t}{4}\left[\frac{1+y_t}{(1-y_t)^2}+\frac{2y_t\ln[y_t]}{(1-y_t)^3}\right]. \tag{24}$$

And finally, the function $L^{(i,H)}$ $(i=1,8)$ describes the charged Higgs contribution [5]

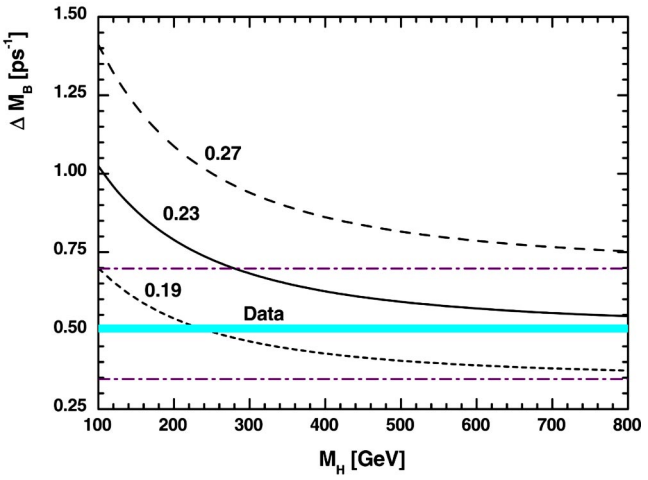

FIG. 3. Plots of the mass splitting ΔM_{B_d} vs charged Higgs boson mass M_H in model III.

$$L^{(i,H)}(x_t,y_t)=2|Y|^2WH^{(i)}(x_t,y_t)+2|Y|^2\Phi H^{(i)}(x_t,y_t)+|Y|^4HH^{(i)}(y_t). \tag{25}$$

The explicit expressions of complicated functions $WH^{(i)}(x_t,y_t)$, $\Phi H^{(i)}(x_t,y_t)$, and $HH^{(i)}(y_t)$ can be found in Ref. [5].

Following Ref. [4], we here use the symbols X and Y to denote the Yukawa couplings between the charged Higgs boson and quarks in the general 2HDMs. In the conventional models I and II, the couplings X and Y are real and given by

$$X=-\cot\beta,\quad Y=\cot\beta\quad(\text{model I}), \tag{26}$$

$$X=\tan\beta,\quad Y=\cot\beta\quad(\text{model II}). \tag{27}$$

In model III where only the couplings λ_{tt} and λ_{bb} are nonzero, the relation between the couplings (X,Y) and $(\lambda_{tt},\lambda_{bb})$ is simple:

$$X=-\lambda_{bb},\quad Y=\lambda_{tt}\quad(\text{model III}). \tag{28}$$

By using the input parameters as given in Appendix A, the SM prediction for ΔM_{B_d} is

$$\Delta M_{B_d}=0.506^{+0.198}_{-0.160}\ \text{ps}^{-1}, \tag{29}$$

where the error comes from the uncertainty of parameter $f_{B_d}\sqrt{\hat{B}_{B_d}}$.

In Fig. 3, we show the M_H dependence of ΔM_{B_d} in model III, assuming $\lambda_{tt}=1$. The region between two horizontal dot-dashed lines corresponds to the SM prediction as given in Eq. (29). The shaded horizontal band shows the world average $\Delta M_{B_d}=0.502\pm0.007\ \text{ps}^{-1}$, and its width corresponds to the error. The short-dashed, solid, and dashed curves in this figure show model III predictions for $f_{B_d}\sqrt{\hat{B}_{B_d}}=0.19,0.23$, and 0.27, respectively.

From the well measured physical observable ΔM_{B_d}, one can find the constraint on $|\lambda_{tt}|$ in model III. In Fig. 4, we

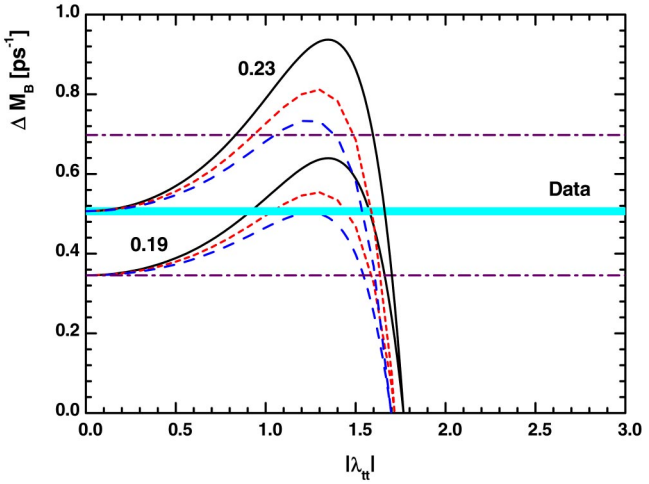

FIG. 4. Plots of the mass splitting ΔM_{B_d} vs $|\lambda_{tt}|$ in model III for $f_{B_d}\sqrt{\hat{B}_{B_d}}=0.19$ (the lower three curves) and $f_{B_d}\sqrt{\hat{B}_{B_d}}=0.23$ (the upper three curves) and for $M_H=200$ (solid curves), 250 (short-dashed curves), and 300 GeV (dashed curves), respectively.

show the $|\lambda_{tt}|$ dependence of ΔM_{B_d} in model III for $f_{B_d}\sqrt{\hat{B}_{B_d}}=0.19$ (the lower three curves) and $f_{B_d}\sqrt{\hat{B}_{B_d}}=0.23$ (the upper three curves) and for $M_H=200$ (solid curves), 250 (short-dashed curves), and 300 GeV (dashed curves), respectively. The shaded band and the region between two horizontal lines are the same as those in Fig. 3. From this figure, an upper bound on $|\lambda_{tt}|$ can be read,

$$|\lambda_{tt}|\leqslant 1.7. \tag{30}$$

This bound is complementary to the constraint obtained from Fig. 5.

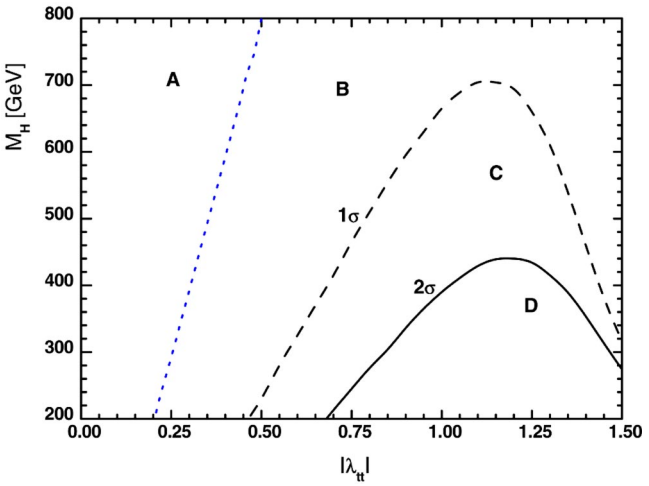

FIG. 5. Contour plot of the mass splitting ΔM_{B_d} in the λ_{tt}-M_H plane. The measured $\Delta M_{B_d}=0.502\pm 0.007$ is used. The A area is allowed by considering the error of ΔM_{B_d} only, but both A and B areas will be allowed if the uncertainty of $f_{B_d}\sqrt{\hat{B}_{B_d}}$ is also taken into account.

Figure 5 is the contour plot of the mass splitting ΔM_{B_d} in the $|\lambda_{tt}|$-M_H plane, where the measured ΔM_{B_d} and the relevant input parameters as given in Appendix A have been used. The area A in Fig. 5 will be allowed by the measured ΔM_{B_d} within 2σ errors (i.e., $\Delta M_{B_d}=0.502\pm 0.014$ ps^{-1}), if we do not consider the effect of the uncertainty of $f_{B_d}\sqrt{\hat{B}_{B_d}}$ in drawing this contour plot. This region corresponds to the allowed region in Fig. 2 of Ref. [18], but much narrow than that one because of the great progress of the experimental measurement of ΔM_{B_d}. If we consider the effect of the large uncertainty of $f_{B_d}\sqrt{\hat{B}_{B_d}}=0.23\pm 0.04$ in our calculations, the areas A plus B in the $|\lambda_{tt}|$-M_H plane will be allowed by the measured ΔM_{B_d} within 1σ error, while the areas A, B, and C will be allowed by the measured ΔM_{B_d} within 2σ errors.

Since the large uncertainty of $f_{B_d}\sqrt{\hat{B}_{B_d}}$ dominate the contour plot, one should take it into account in the effort to limit the free parameters in model III. As discussed previously, the uncertainty of $|V_{td}|$ is strongly correlated with the uncertainty of $f_{B_d}\sqrt{\hat{B}_{B_d}}$, and we therefore consider the uncertainty of $f_{B_d}\sqrt{\hat{B}_{B_d}}$ but use the central value $|V_{td}|=0.0079$ in our calculation.

For the sake of experimental searches, one prefers a relatively light charged Higgs boson. From the contour plot Fig. 5, the region of $|\lambda_{tt}|\gtrsim 0.7$ is disfavored if we expect existence of a light charged Higgs boson, while the parameter space of

$$|\lambda_{tt}|\approx 0.5 \quad \text{and} \quad M_H\approx 200 \ \text{GeV} \tag{31}$$

is certainly allowed by the measured mass splitting ΔM_{B_d}. The allowed region in the contour plot will become narrow along with further improvement of the data and reduction of the large theoretical uncertainty of parameter $f_{B_d}\sqrt{\hat{B}_{B_d}}$.

Since the new physics contributions to ΔM_{B_d} depend on $|Y|^2$ and $|Y|^4$ only, the charged Higgs contributions in models II and III will be the same if we use the same value of the Yakawa coupling $|Y|$ as input. In model II, we have $Y=1/\tan\beta$. The upper limit on $|\lambda_{tt}|$ as given in Eq. (30) can be translated to a lower limit on $\tan\beta$,

$$\tan\beta\geqslant 0.6, \tag{32}$$

as can be seen directly from Fig. 6, where the upper and lower three curves correspond to $f_{B_d}\sqrt{\hat{B}_{B_d}}=0.19$ and 0.23, respectively. The solid, short-dashed, and dashed curves correspond to the model III prediction for $M_H=200$, 250, and 300 GeV, respectively. The shaded band and the region between two horizontal lines are the same as those in Fig. 3. One can also see from this figure that the new physics contribution become negligible for $\tan\beta\geqslant 5$.

IV. THE DECAY $B\to X_s\gamma$ IN MODEL III

In the absence of new light degrees of freedom, the new physics contributions to the rare decay $B\to X_s\gamma$ will manifest

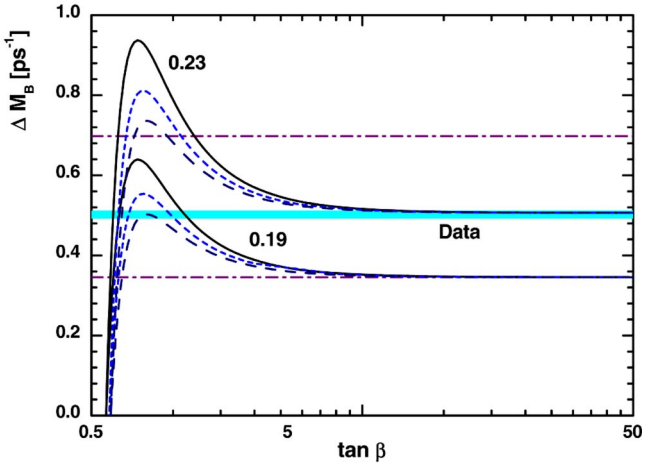

FIG. 6. Plots of the mass splitting ΔM_{B_d} vs $\tan\beta$ in model II for $f_{B_d}\sqrt{\hat{B}_{B_d}}=0.19$ (the lower three curves) and $f_{B_d}\sqrt{\hat{B}_{B_d}}=0.23$ (the upper three curves) and for $M_H=200$ (solid curves), 250 (short-dashed curves), and 300 GeV (dashed curves), respectively. For details, see text.

itself through the new contributions to the Wilson coefficients of the same operators involved in the SM calculation, or the new operators absent in the SM, such as operators with different chirality. The excellent agreement between SM theory and experimental data leads to strong constraints on many new physics models beyond the SM.

In this section, we calculate the branching ratio $\mathcal{B}(B \to X_s\gamma)$ in model III. Here, the operator basis in the SM and model III under study is the same. The NLO QCD corrections will be included in model III by extending the calculations in Ref. [4]. As a comparison, we also give the numerical results in model II where it is necessary.

A. Effective Hamiltonian and operator basis

In the framework of the SM, if we only take into account operators up to dimension 6 and put $m_s=0$, the effective Hamiltonian for $b\to s\gamma$ at the scale μ reads [4]

$$\mathcal{H}_{eff}=-\frac{4G_F}{\sqrt{2}}V_{ts}V_{tb}^*\sum_{i=1}^{8}C_i(\mu)O_i(\mu). \tag{33}$$

The operator basis introduced by Chetyrkin, Misiak, and Münz[3] (CMM) are given by

$$\mathcal{O}_1=(\bar{s}_L\gamma_\mu T^a c_L)(\bar{c}_L\gamma^\mu T_a b_L), \tag{34}$$

$$\mathcal{O}_2=(\bar{s}_L\gamma_\mu c_L)(\bar{c}_L\gamma^\mu b_L), \tag{35}$$

$$\mathcal{O}_3=(\bar{s}_L\gamma_\mu b_L)\sum_q(\bar{q}\gamma^\mu q), \tag{36}$$

$$\mathcal{O}_4=(\bar{s}_L\gamma_\mu T^a b_L)\sum_q(\bar{q}\gamma^\mu T_a q), \tag{37}$$

$$\mathcal{O}_5=(\bar{s}_L\gamma_\mu\gamma_\nu\gamma_\rho b_L)\sum_q(\bar{q}\gamma^\mu\gamma^\nu\gamma^\rho q), \tag{38}$$

$$\mathcal{O}_6=(\bar{s}_L\gamma_\mu\gamma_\nu\gamma_\rho T^a b_L)\sum_q(\bar{q}\gamma^\mu\gamma^\nu\gamma^\rho T_a q), \tag{39}$$

$$\mathcal{O}_7=\frac{e}{16\pi^2}\bar{m}_b(\mu)(\bar{s}_L\sigma^{\mu\nu}b_R)F_{\mu\nu}, \tag{40}$$

$$\mathcal{O}_8=\frac{g_s}{16\pi^2}\bar{m}_b(\mu)(\bar{s}_L\sigma^{\mu\nu}T^a b_R)G^a_{\mu\nu}, \tag{41}$$

where T_a $(a=1,\ldots,8)$ stands for $SU(3)_c$ generators, g_s and e are the strong and electromagnetic coupling constants, $L,R=(1\mp\gamma_5)/2$ for the left and right-handed projection operators, O_1 and O_2 are current-current operators, O_3–O_6 are the QCD penguin operators, and O_7 and O_8 are electromagnetic and chromomagnetic penguin operators. In Eq. (41), $\bar{m}_b(\mu)$ is the running b-quark mass in the modified minimal subtraction ($\overline{\rm MS}$) scheme at the renormalization scale μ (see Appendix A for details).

B. NLO Wilson coefficients at the scale μ_W and μ_b

To the first order in α_S, the effective Wilson coefficients at the scale $\mu_W=\mathcal{O}(M_W)$ can be written as [4]

$$C_i^{\rm eff}(\mu_W)=C_i^{0,\rm eff}(\mu_W)+\frac{\alpha_S(\mu_W)}{4\pi}C_i^{1,\rm eff}(\mu_W). \tag{42}$$

The LO Wilson coefficients at the matching energy scale M_W take the form [4]

$$C_2^{0,\rm eff}(\mu_W)=1, \tag{43}$$

$$C_i^{0,\rm eff}(\mu_W)=0 \quad (i=1,3,4,5,6), \tag{44}$$

$$C_7^{0,\rm eff}(\mu_W)=C_{7,SM}^0(M_W)+|Y|^2C_{7,YY}^0(M_W)+(XY^*)C_{7,XY}^0(M_W), \tag{45}$$

$$C_8^{0,\rm eff}(\mu_W)=C_{8,SM}^0(M_W)+|Y|^2C_{8,YY}^0(M_W)+(XY^*)C_{8,XY}^0(M_W), \tag{46}$$

with

$$C_{7,SM}^0=\frac{3x_t^3-2x_t^2}{4(x_t-1)^4}\ln x_t+\frac{-8x_t^3-5x_t^2+7x_t}{24(x_t-1)^3}, \tag{47}$$

$$C_{8,SM}^0=\frac{-3x_t^2}{4(x_t-1)^4}\ln x_t+\frac{-x_t^3+5x_t^2+2x_t}{8(x_t-1)^3}, \tag{48}$$

[3]There are two popular operator basis used in literature. The standard basis was defined, for example, in Ref. [34]. The second one is the CMM basis, where the fully anticommuting γ_5 in dimensional regularization is employed [6].

$$C^0_{7,YY}=\frac{3y_t^3-2y_t^2}{12(y_t-1)^4}\ln y_t+\frac{-8y_t^3-5y_t^2+7y_t}{72(y_t-1)^3}, \tag{49}$$

$$C^0_{7,XY}=\frac{y_t}{12}\left[\frac{-5y_t^2+8y_t-3+(6y_t-4)\ln y_t}{(y_t-1)^3}\right], \tag{50}$$

$$C^0_{8,YY}=\frac{-3y_t^2}{12(y_t-1)^4}\ln y_t+\frac{-y_t^3+5y_t^2+2y_t}{24(y_t-1)^3}, \tag{51}$$

$$C^0_{8,XY}=\frac{y_t}{4}\left[\frac{-y_t^2+4y_t-3-2\ln y_t}{(y_t-1)^3}\right], \tag{52}$$

where $x_t=m_t^2/M_W^2$, $y_t=m_t^2/M_H^2$, and these leading order functions have no explicit μ_W dependence.

The NLO Wilson coefficients at the matching scale μ_W in model III can be written as [4]

$$C_1^{1,\mathrm{eff}}(\mu_W)=15+6\ln\frac{\mu_W^2}{M_W^2}, \tag{53}$$

$$C_4^{1,\mathrm{eff}}(\mu_W)=E_0+\frac{2}{3}\ln\frac{\mu_W^2}{M_W^2}+|Y|^2E_H, \tag{54}$$

$$C_i^{1,\mathrm{eff}}(\mu_W)=0 \quad (i=2,3,5,6), \tag{55}$$

$$C_7^{1,\mathrm{eff}}(\mu_W)=C^1_{7,SM}(\mu_W)+|Y|^2C^1_{7,YY}(\mu_W)+(XY^*)C^1_{7,XY}(\mu_W), \tag{56}$$

$$C_8^{1,\mathrm{eff}}(\mu_W)=C^1_{8,SM}(\mu_W)+|Y|^2C^1_{8,YY}(\mu_W)+(XY^*)C^1_{8,XY}(\mu_W), \tag{57}$$

where for $i=7,8$ the functions on the right-hand side of Eqs. (56) and (57) are

$$C^1_{i,SM}(\mu_W)=W_{i,SM}+M_{i,SM}\ln\frac{\mu_W^2}{M_W^2}+T_{i,SM}\left(\ln\frac{m_t^2}{\mu_W^2}-\frac{4}{3}\right), \tag{58}$$

$$C^1_{i,YY}(\mu_W)=W_{i,YY}+M_{i,YY}\ln\frac{\mu_W^2}{M_H^2}+T_{i,YY}\left(\ln\frac{m_t^2}{\mu_W^2}-\frac{4}{3}\right), \tag{59}$$

$$C^1_{i,XY}(\mu_W)=W_{i,XY}+M_{i,XY}\ln\frac{\mu_W^2}{M_H^2}+T_{i,XY}\left(\ln\frac{m_t^2}{\mu_W^2}-\frac{4}{3}\right). \tag{60}$$

The explicit expressions of functions $W_{i,j}$, $M_{i,j}$, and $T_{i,j}$ ($i=7,8$ and $j=SM,YY,XY$) can be found in Ref. [4], and also listed in Appendix B for the convenience of the reader.

The new physics contributions to the $B\to X_s\gamma$ decay are described by the functions $C^{0,1}_{i,j}(\mu_W)$ with $i=(7,8)$ and $j=(YY,XY)$ as defined in Eqs. (49)–(52), (59), and (60). These eight functions depend on the unknown M_H and the well measured M_W and m_t only, and show clear decoupling behavior when M_H approaches infinity, as illustrated in Fig. 7 for the four functions $C^{0,1}_{7,YY}(M_W)$ and $C^{0,1}_{7,XY}(M_W)$. The other four functions $C^{0,1}_{8,YY}(M_W)$ and $C^{0,1}_{8,XY}(M_W)$ have very similar decoupling behavior. Numerically, the LO new physics functions $C^0_{i,j}(M_W)$ are always negative and have the same sign with their SM counterparts, while the NLO new physics functions $C^1_{i,j}(M_W)$ are always positive and have the opposite sign of their SM counterparts.

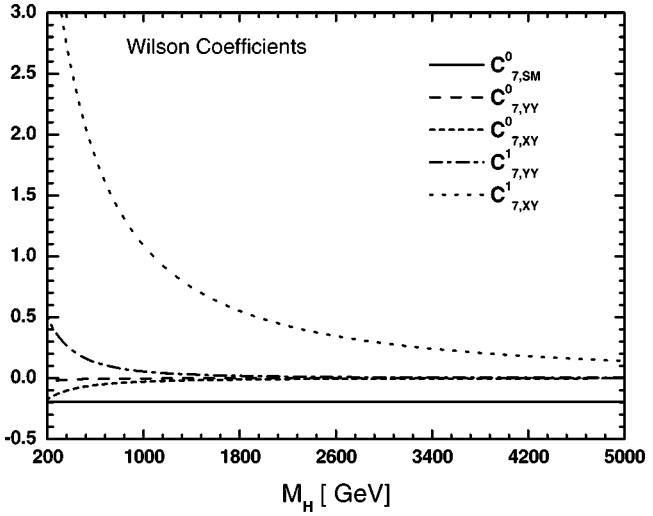

FIG. 7. Plots of M_H dependence of $C^0_{7,SM}(M_W)$ (solid line) and the four functions $C^{0,1}_{7,YY}(M_W)$ (the dashed and dot-dashed curves) and $C^{0,1}_{7,XY}(M_W)$ (the short-dashed and dotted curves). The decoupling behavior of new physics contributions can be seen clearly.

Of course, the new physics contributions to $B\to X_s\gamma$ also depend on the size and sign of the couplings X and Y, as can be seen easily from Eqs. (49)–(52), (59), and (60). For the conventional model II, we have

$$|Y|^2=\frac{1}{\tan^2\beta}, \quad XY^*=1, \tag{61}$$

from the definition of X and Y as given in Eq. (27). For the model III under study, we have

$$|Y|^2=|\lambda_{tt}|^2, \quad XY^*=-|\lambda_{tt}||\lambda_{bb}|e^{i\theta}, \tag{62}$$

where $\theta=\theta_b-\theta_t$ is the relative phase of the coupling λ_{tt} and λ_{bb} in model III. The sign of the second term in above equation can be negative or positive depending on the choice of θ. In numerical calculations, we generally set $\theta=0°$, unless otherwise specified, and will study the effects of a nonzero θ in the end of this section.

Since the heavy charged Higgs bosons have been integrated out at the scale μ_W, the QCD running of the Wilson coefficients $C_i(\mu_W)$ down to the lower energy scale $\mu_b=\mathcal{O}(m_b)$ after including the new physics contributions is the

TABLE I. The "magic numbers" appearing in the calculations of the Wilson coefficients $C_i(\mu)$ in the rare decay $b\to s\gamma$.

i	1	2	3	4	5	6	7	8
a_i	$\frac{14}{23}$	$\frac{16}{23}$	$\frac{6}{23}$	$-\frac{12}{23}$	0.4086	−0.4230	−0.8994	0.1456
h_{1i}	0	0	1	−1	0	0	0	0
h_{2i}	0	0	$\frac{2}{3}$	$\frac{1}{3}$	0	0	0	0
h_{3i}	0	0	$\frac{2}{63}$	$-\frac{1}{27}$	−0.0659	0.0595	−0.0218	0.0335
h_{4i}	0	0	$\frac{1}{21}$	$\frac{1}{9}$	0.0237	−0.0173	−0.01336	−0.0136
h_{5i}	0	0	$-\frac{1}{126}$	$\frac{1}{108}$	0.0094	−0.01	0.001	−0.0017
h_{6i}	0	0	$-\frac{1}{84}$	$-\frac{1}{36}$	0.0108	0.0163	0.0103	0.0023
e_i	$\frac{4661194}{816831}$	$-\frac{8516}{2217}$	0	0	−1.9043	−0.1008	0.01216	0.0183
f_i	−17.3023	8.5027	4.5508	0.7519	2.0040	0.7476	−0.5358	0.0914
k_i	9.9372	−7.4878	1.2688	−0.2925	−2.2923	−0.1461	0.1239	0.0812
l_i	0.5784	−0.3921	−0.1429	0.0476	−0.1275	0.0317	0.0078	−0.0031
h_i	2.2996	−1.0880	$-\frac{3}{7}$	$-\frac{1}{14}$	−0.6494	−0.0380	−0.0185	−0.0057
$\hbar_i$	0.8623	0	0	0	−0.9135	0.0873	−0.0571	0.0209
$\gamma_{i7}^{0,\mathrm{eff}}$	$-\frac{208}{243}$	$\frac{416}{81}$	$-\frac{176}{81}$	$-\frac{152}{243}$	$-\frac{6272}{81}$	$\frac{4624}{243}$	$\frac{32}{3}$	$-\frac{32}{9}$

same as in the SM. For a complete NLO analysis of the radiative decay $B\to X_s\gamma$, only the Wilson coefficient $C_7^{\mathrm{eff}}(\mu_b)$ is known to NLO precision,

$$C_7^{\mathrm{eff}}(\mu_b)=C_7^{0,\mathrm{eff}}(\mu_b)+\frac{\alpha_S(\mu_b)}{4\pi}C_7^{1,\mathrm{eff}}(\mu_b), \tag{63}$$

with

$$C_7^{0,\mathrm{eff}}(\mu_b)=\eta^{16/23}C_7^{0,\mathrm{eff}}(\mu_W)+\frac{8}{3}(\eta^{14/23}-\eta^{16/23})C_8^{0,\mathrm{eff}}(\mu_W)+\sum_{i=1}^{8}h_i\eta^{a_i}C_2^{0,\mathrm{eff}}(\mu_W), \tag{64}$$

$$\begin{aligned}C_7^{1,\mathrm{eff}}(\mu_b)=&\eta^{39/23}C_7^{1,\mathrm{eff}}(\mu_W)+\frac{8}{3}(\eta^{37/23}-\eta^{39/23})C_8^{1,\mathrm{eff}}(\mu_W)\\&+\left(\frac{297664}{14283}\eta^{16/23}-\frac{7164416}{357075}\eta^{14/23}+\frac{256868}{14283}\eta^{37/23}-\frac{6698884}{357075}\eta^{39/23}\right)C_8^{0,\mathrm{eff}}(\mu_W)\\&+\frac{37208}{4761}(\eta^{39/23}-\eta^{16/23})C_7^{0,\mathrm{eff}}(\mu_W)\\&+\sum_{i=1}^{8}[e_i\eta C_4^{1,\mathrm{eff}}(\mu_W)+f_i+k_i\eta+l_i\eta C_1^{1,\mathrm{eff}}(\mu_W)]\eta^{a_i},\end{aligned} \tag{65}$$

where the symbol η is defined as $\eta=\alpha_s(\mu_W)/\alpha_s(\mu_b)$, and the "magic numbers" a_i, h_i, e_i, f_i, k_i, and l_i in Eq. (65) are listed in Table I.

The remaining coefficients are only needed to LO precision,

$$C_j^{0,\mathrm{eff}}(\mu_b)=\sum_{i=1}^{8}h_{ji}\eta^{a_i}\quad\text{for } j=1,\ldots,6, \tag{66}$$

$$C_8^{0,\mathrm{eff}}(\mu_b)=\eta^{14/23}C_8^{0,\mathrm{eff}}(\mu_W)+\sum_{i=1}^{8}\hbar_i\eta^{a_i}, \tag{67}$$

where the magic numbers $\hbar_i$ and h_{ji} are also listed in Table I. Following Ref. [4], the small coefficients $C_3^{0,\mathrm{eff}}(\mu_b),\ldots,C_6^{0,\mathrm{eff}}(\mu_b)$ will be neglected in numerical calculations.

C. Branching ratio $\mathcal{B}(B\to X_s\gamma)$ in the SM

The branching ratio of the inclusive radiative decay $B\to X_s\gamma$ can be written as

$$\mathcal{B}(B\to X_s\gamma)_{LO}=\mathcal{B}_{SL}\left|\frac{V_{ts}^*V_{tb}}{V_{cb}}\right|^2\frac{6\alpha_{em}}{\pi f(z)}|C_7^{0,eff}(\mu_b)|^2, \tag{68}$$

at the LO level, and

$$\mathcal{B}(B\to X_s\gamma)_{NLO}=\mathcal{B}_{SL}\left|\frac{V_{ts}^*V_{tb}}{V_{cb}}\right|^2\frac{6\alpha_{em}}{\pi f(z)\kappa(z)}[|\bar{D}|^2+A+\Delta], \tag{69}$$

at the NLO level, where $\mathcal{B}_{SL}=(10.64\pm0.23)\%$ is the measured semileptonic branching ratio of the B meson [2], $\alpha_{em}=1/137.036$ is the fine-structure constant,[4] $z=m_c^{pole}/m_b^{pole}=0.29\pm0.02$ is the ratio of the quark pole mass,[5] and $f(z)$

[4]Based on the analysis in Ref. [35], it is more appropriate to use $\alpha_{em}^{-1}=137.036$ instead of $\alpha_{em}^{-1}=130.3\pm2.3$ in the study of $B\to X_s\gamma$ decay.

[5]Another choice of z is $z=\overline{m}_c(\mu)/m_b^{pole}=0.22\pm0.04$, but we do not consider this issue here. For more details about quark mass effects in $B\to X_s\gamma$ decay, see Ref. [9].

and $\kappa(z)$ denote the phase space factor and the QCD correction [36] for the semileptonic B decay:

$$f(z)=1-8z^2+8z^6-z^8-24z^4\log(z), \tag{70}$$

$$\kappa(z)=1-\frac{2\alpha_s(\mu)}{3\pi}\left[\left(\pi^2-\frac{31}{4}\right)(1-z)^2+\frac{3}{2}\right]+\frac{\delta_{SL}^{NP}}{m_b^2}, \tag{71}$$

where δ_{SL}^{NP} denotes the nonperturbative correction to the semileptonic B meson decay,

$$\delta_{SL}^{NP}=\frac{\lambda_1}{2}+\frac{3}{2}\lambda_2\left[1-4\frac{(1-z^2)^4}{f(z)}\right]. \tag{72}$$

The term $\overline{D}$ in Eq. (69) corresponds to the subprocesses $b\to s\gamma$ [4]

$$\overline{D}=C_7^{\rm eff}(\mu_b)+V(\mu_b), \tag{73}$$

where the NLO Wilson coefficient $C_7^{\rm eff}(\mu_b)$ has been given in Eq. (63), and the function $V(\mu_b)$ is defined as

$$V(\mu_b)=\frac{\alpha_S(\mu_b)}{4\pi}\left\{\sum_{i=1}^{8}C_i^{0,\rm eff}(\mu_b)\left[r_i+\frac{1}{2}\gamma_{i7}^{0,\rm eff}\ln\frac{m_b^2}{\mu_b^2}\right]-\frac{16}{3}C_7^{0,\rm eff}(\mu_b)\right\}, \tag{74}$$

where the functions r_i $(i=1,\ldots,8)$ are the virtual correction functions (see Appendix D of Ref. [4]), and $\gamma_{i7}^{0,\rm eff}$ are the elements of the anomalous dimension matrix that govern the evolution of the Wilson coefficients from the matching scale μ_W to lower scale μ_b. The values of $\gamma_{i7}^{0,\rm eff}$ have been given in the last line of Table I; for details see Ref. [34]. The LO Wilson coefficients in Eq. (74) have been given in previous subsections.

In Eq. (69), term A is the correction coming from the bremsstrahlung process $b\to s\gamma g$ [37]

$$A=\frac{\alpha_s(\mu_b)}{\pi}\sum_{i,j=1;i\leqslant j}^{8}{\rm Re}\{C_i^{0,\rm eff}(\mu_b)[C_j^{0,\rm eff}(\mu_b)]^* f_{ij}\}. \tag{75}$$

The coefficients f_{ij} have been defined and computed in Refs. [6,37]. We here use the explicit expressions of those relevant f_{ij} as given in Appendix E of Ref. [4].

In order to relate the quark decay rate to the actual hadronic process, the nonperturbative corrections obtained with the method of the heavy-quark effective theory (HQET) should be included. The term Δ in Eq. (69) and the term δ_{SL}^{NP} in Eq. (71) denote these nonperturbative corrections, which scale as $1/m_b^2$ and $1/m_c^2$ [38,39],

$$\Delta=\frac{\delta_\gamma^{NP}}{m_b^2}|C_7^{0,eff}(\mu_b)|^2+\frac{\delta_c^{NP}}{m_c^2}{\rm Re}\left\{[C_7^{0,eff}(\mu_b)]^*\left[C_2^{0,eff}(\mu_b)-\frac{1}{6}C_1^{0,eff}(\mu_b)\right]\right\}, \tag{76}$$

with

$$\delta_\gamma^{NP}=\frac{\lambda_1}{2}-\frac{9}{2}\lambda_2, \tag{77}$$

$$\delta_c^{NP}=-\frac{\lambda_2}{9}, \tag{78}$$

where $\lambda_2=(m_{B^*}^2-m_B^2)/4=0.12\ {\rm GeV}^2$ extracted from the B meson mass splitting, while the parameter $\lambda_1=0.5\ {\rm GeV}^2$ has a large uncertainty but the overall λ_1 dependence largely cancels in the decay rate with the λ_1 term in δ_{SL}^{NP} as can be seen from Eq. (69).

Now we are ready to present numerical results of the branching ratios in the SM and 2HDMs, specifically in model III. For the numerical evaluations, unless otherwise specified, we use the central value of input parameters given in Appendix A. For the values of the matching scale and low energy scale, we always take $\mu_W=M_W$ and $m_b/2\leqslant\mu_b\leqslant 2m_b$.

Using Eq. (69), we find the SM prediction of the branching ratio $\mathcal{B}(B\to X_s\gamma)$,

$$\begin{aligned}\mathcal{B}(B\to X_s\gamma)_{NLO}^{SM}=&\left[3.52^{+0.02}_{-0.16}(\mu_b)\pm 0.08(\mathcal{B}_{SL})^{+0.20}_{-0.16}\left(\frac{m_c}{m_b}\right)\right.\\&\left.\pm 0.13(\alpha_s)\pm 0.05(m_t)\pm 0.04\left(\left|\frac{V_{ts}^*V_{tb}}{V_{cb}}\right|^2\right)\right]\\&\times 10^{-4}\\=&(3.52\pm 0.28)\times 10^{-4},\end{aligned} \tag{79}$$

where the major sources of errors are shown explicitly, and the individual errors are added in quadrature. The central value 3.52×10^{-4} is obtained by using the central values of input parameters listed in Appendix A and setting $\mu_W=M_W$ and $\mu_b=m_b$. In this paper, we only consider the effects of the uncertainties of those six parameters as specified in Eq. (79).

D. Branching ratio $\mathcal{B}(B\to X_s\gamma)$ in model III

In the model III considered in this paper, the branching ratio has been parametrized in terms of the three parameters $\lambda_{tt},\lambda_{bb}$, and M_H. From the limit on $|\lambda_{tt}|$ obtained from the measured mass splitting ΔM_{B_d}, the magnitude of the coupling λ_{tt} should be smaller than 1 if we require the charged Higgs boson to be relatively light, as can be seen from Fig. 5. In this section, we always set $|\lambda_{tt}|=0.5$, unless otherwise specified.

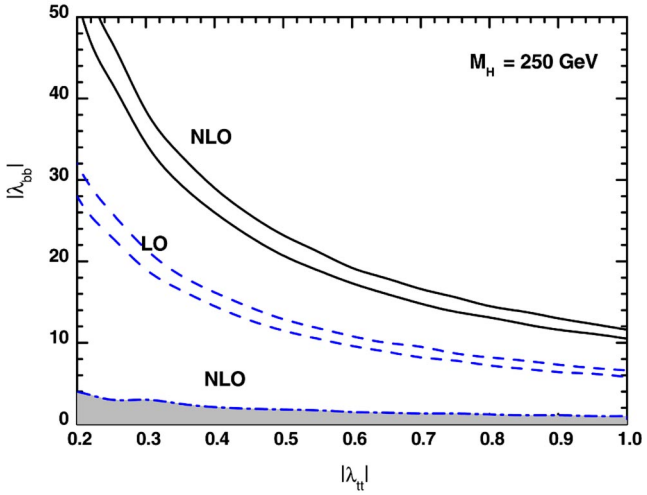

FIG. 8. Contour plot of the branching ratio $\mathcal{B}(B\to X_s\gamma)$ in the $|\lambda_{tt}|$-$|\lambda_{bb}|$ plane, assuming $M_H=250$ GeV.

We first check the common allowed regions in $|\lambda_{tt}|$-$|\lambda_{bb}|$ plane for given $M_H=250$ GeV. Figure 8 is the contour plot in the $|\lambda_{tt}|$-$|\lambda_{bb}|$ plane by using the LO and NLO theoretical predictions in model III and the measured branching ratio at the 2σ level: $2.58\times10^{-4}\leq\mathcal{B}(B\to X_s\gamma)\leq4.1\times10^{-4}$. In this contour plot, the first allowed region is the shaded area close to the X axis where both $|\lambda_{tt}|$ and $|\lambda_{bb}|$ are all small, which is obtained when the NLO theoretical prediction is employed. The second allowed region is the area between two dashed curves obtained when the LO theoretical prediction is employed. The third region is the region between two solid curves allowed when the NLO theoretical prediction is employed.

We choose one point of $(\lambda_{tt},\lambda_{bb})$ in each of three allowed regions of Fig. 8 as typical choices:

$$\begin{aligned}&\text{Case A:}\quad (\lambda_{tt},\lambda_{bb})=(0.5,1),\\ &\text{Case B:}\quad (\lambda_{tt},\lambda_{bb})=(0.5,12),\\ &\text{Case C:}\quad (\lambda_{tt},\lambda_{bb})=(0.5,22),\end{aligned}\tag{80}$$

which will be used as input in the following numerical calculations. Here the limit on $|\lambda_{tt}|$ from the measured ΔM_{B_d} as studied in last section has been taken into account.

Since the new physics contribution to the decay $B\to X_s\gamma$ is incorporated through its correction to the Wilson coefficients $C_{7,8}^{0,1}(\mu_W)$, we would like to check the size and sign of the new physics parts and their relative strength to the SM part, to show the theoretical features of the NLO contributions and to draw the constraint on M_H by comparing the theoretical predictions with the data.

1. Case A

We firstly consider the case A: $(\lambda_{tt},\lambda_{bb})=(0.5,1)$. Using the input parameters as given in Appendix A and assuming $M_H=250$ GeV, we find the numerical results of $C_7^{0,1}$

$$C_7^{0,\mathrm{eff}}(M_W)=\underbrace{-0.1952}_{C_{7,SM}^{0,\mathrm{eff}}(M_W)}\quad\underbrace{-0.0057}_{|Y|^2C_{7,YY}^{0,\mathrm{eff}}(M_W)}\quad\underbrace{+0.0730}_{(XY^*)C_{7,XY}^{0,\mathrm{eff}}(M_W)}=-0.1280,\tag{81}$$

$$C_7^{1,\mathrm{eff}}(M_W)=\underbrace{-2.3712}_{C_{7,SM}^{1,\mathrm{eff}}(M_W)}\quad\underbrace{+0.1013}_{|Y|^2C_{7,YY}^{1,\mathrm{eff}}(M_W)}\quad\underbrace{-1.7239}_{(XY^*)C_{7,XY}^{1,\mathrm{eff}}(M_W)}=-3.9942,\tag{82}$$

at the matching scale $\mu_W=M_W$, and

$$C_7^{\mathrm{eff}}(m_b)=\underbrace{-0.3137}_{C_{7,SM}^{0,\mathrm{eff}}(m_b)}\quad\underbrace{+0.0082}_{\Delta C_{7,SM}^{1}(m_b)}\quad\underbrace{+0.0507}_{C_{7,NP}^{0,\mathrm{eff}}(m_b)}\quad\underbrace{-0.0142}_{\Delta C_{7,NP}^{1}(m_b)}=-0.2690,\tag{83}$$

at the lower scale $\mu_b=m_b$, where $\Delta C_{7,j}^1(\mu)=[\alpha_S(\mu)/4\pi]C_{7,j}^{1,\mathrm{eff}}(\mu)$ and $j=(\mathrm{SM,NP})$ denotes the NLO QCD corrections to the corresponding Wilson coefficients. It is easy to see the following:

(1) As shown in Eqs. (81) and (82), the new physics contributions proportional to $|Y|^2$ and XY^* have the opposite sign and will cancel each other to some degree. The net new physics contribution is relatively small and has the opposite sign with its SM counterpart.

(2) The net NLO new physics contribution has the same

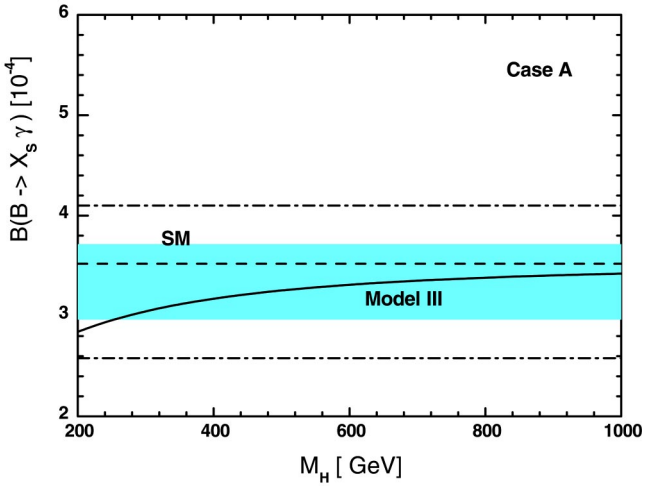

FIG. 9. The M_H dependence of the branching ratio $\mathcal{B}(B\to X_s\gamma)$ for case A: $(\lambda_{tt},\lambda_{bb})=(0.5,1)$ at the NLO level. The band between two horizontal dot-dashed lines shows the data at 2σ level. The dashed line and solid curve refer to the SM and model III predictions, respectively.

sign and is comparable in size to its SM counterpart.

(3) At the low energy scale $\mu_b=\mathcal{O}(m_b)$, the LO and NLO new physics contributions to $C_7^{\rm eff}(m_b)$ have the opposite sign; they will cancel each other. The total Wilson coefficient $C_7^{\rm eff}(m_b)$ as given in Eq. (83) remains negative but changes from -0.3055 to -0.2690 (about a 12% decrease in magnitude) after the cancellation due to the new physics part.

(4) The new physics corrections are generally small in magnitude, since the couplings X and Y are all relatively small for case A.

Explicit calculations also show that the new physics corrections to V_{m_b},A, and Δ terms are induced through the modification to the Wilson coefficients $C_{7,8}^{0,\rm eff}(\mu_b)$. But for case A, such corrections are small in size and therefore the theoretical prediction for the branching ratio $\mathcal{B}(B\to X_s\gamma)$ in this case agrees well with the data within 1σ error, as illustrated in Fig. 9. The region between two dot-dashed lines and the shaded part in Fig. 9 shows the measured branching ratio with 2σ and 1σ error, respectively. The dashed line and solid curve show the central value of the SM and model III (case A) prediction, respectively.

Obviously, the theoretical prediction of case A agrees well with both the SM prediction and the data because both λ_{tt} and λ_{bb} are small in size. But this case is not interesting theoretically, since the new physics effect is too small to be separated from the SM contribution through experiments.

2. Case B

Now we turn to case B: $(\lambda_{tt},\lambda_{bb})=(0.5,12)$. Here only leading order contributions in both SM and model III are taken into account, and the branching ratio $\mathcal{B}(B\to X_s\gamma)$ is completely determined by the Wilson coefficient $C_7^{0,eff}(\mu_b)$ as shown in Eq. (68).

Using the input parameters as given in Appendix A and assuming $M_H=250$ GeV, we find numerically that

$$C_7^{0,\rm eff}(M_W)=\underbrace{-0.1952}_{C_{7,SM}^{0,\rm eff}(M_W)}\quad\underbrace{-0.0057}_{|Y|^2C_{7,YY}^{0,\rm eff}(M_W)}\quad\underbrace{+0.8754}_{(XY^*)C_{7,XY}^{0,\rm eff}(M_W)}=0.6475 \tag{84}$$

at the matching scale $\mu_W=M_W$, and

$$C_7^{0,\rm eff}(m_b)=\underbrace{-0.3137}_{C_{7,SM}^{0,\rm eff}(m_b)}\quad\underbrace{-0.0042}_{C_{7,YY}^{0,\rm eff}(m_b)}\quad\underbrace{+0.6581}_{C_{7,XY}^{0,\rm eff}(m_b)}=+0.3402, \tag{85}$$

at the lower scale $\mu_b=m_b$. It is easy to see the following from the numbers as given in Eqs. (84) and (85):

(a) The new physics contribution proportional to the XY^* term is much larger in size than the one proportional to X.

b) At both energy scales M_W and m_b, the net new physics contributions to $C_7^{0,\rm eff}(\mu)$ are always positive and much larger in magnitude than its SM counterpart. The total LO Wilson coefficient $C_7^{0,\rm eff}(m_b)$ changed from -0.3137 in the SM to $+0.3402$ in model III.

From the $B\to X_s\gamma$ decay, only the magnitude of $C_7(m_b)$ instead of its sign can be constrained by the relevant data. The semileptonic decay $B\to K^{(*)}l^+l^-$ is sensitive to the sign of C_7, but the precision of the measurement is still not high enough to determine the sign of C_7.

In Fig. 10, we show the M_H dependence of the branching ratio for case B. The dashed line shows the LO SM prediction $\mathcal{B}(B\to X_s\gamma)=2.61\times10^{-4}$, while the solid curve shows the model III prediction for case B. It is interesting to note that the LO SM prediction is marginally consistent with the data within 2σ errors, but the NLO SM prediction agrees perfectly with the data.

One can also find the limit on M_H, $228\leqslant M_H$

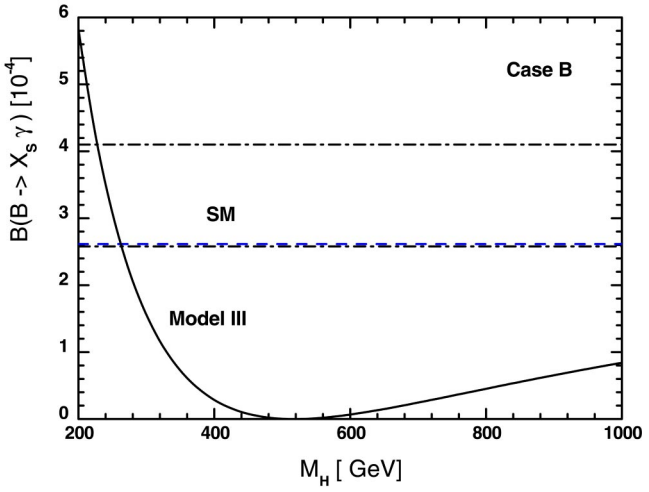

FIG. 10. The M_H dependence of the branching ratio $\mathcal{B}(B \to X_s\gamma)$ for case B: $(\lambda_{tt},\lambda_{bb})=(0.5,12)$ at the LO level. The band between two horizontal dot-dashed lines shows the data at the 2σ level. The dashed line and solid curve refers to the SM and model III predictions, respectively.

$\leqslant 264$ GeV, from Fig. 10 directly. But one should know that the values of the lower and upper limits on M_H will change along with the variation of λ_{tt} and λ_{bb}. The point here is that a relatively light charged Higgs boson is still allowed in model III even at the leading order.

3. Case C

For case C, the LO and NLO new physics contributions to the Wilson coefficients $C_7(M_W)$ and $C_8(M_W)$ are rather large. For given $(\lambda_{tt},\lambda_{bb})=(0.5,22)$ and assuming $M_H=250$ GeV, we find numerically that

$$C_7^{0,\mathrm{eff}}(M_W) = -0.1952 + 1.5992 = +1.4040, \tag{86}$$

$$C_8^{0,\mathrm{eff}}(M_W) = -0.0972 + 1.4815 = +1.3843, \tag{87}$$

$$\frac{\alpha_s(M_W)}{4\pi} C_7^{1,\mathrm{eff}}(M_W) = -0.0229 - 0.3652 = -0.3881, \tag{88}$$

$$\frac{\alpha_s(M_W)}{4\pi} C_8^{1,\mathrm{eff}}(M_W) = -0.0209 - 0.2372 = -0.2580, \tag{89}$$

where the first and second terms denote the SM and the new physics contributions, respectively. Clearly, the new physics contributions are always much larger than their SM counterparts in magnitude.

After the inclusion of new physics contributions, the coefficients $C_7^{0,\mathrm{eff}}(M_W)$ and $C_8^{0,\mathrm{eff}}(M_W)$ become large and positive. For NLO contributions, the new physics parts are around 10 times larger than the corresponding SM parts. Among the new physics parts, the contribution proportional to the term XY^* is absolutely dominant over the one proportional to $|Y|^2$, for example,

$$|\lambda_{tt}|^2 C_{7,YY}^0(M_W) = -0.0057,$$

$$-|\lambda_{tt}||\lambda_{bb}| C_{7,XY}^0(M_W) = 1.605 \tag{90}$$

for case C and $M_H=250$ GeV, since $|\lambda_{bb}|$ is now 40 times larger than $|\lambda_{tt}|$.

Putting these findings together, we find numerically that

$$C_7^{\mathrm{eff}}(M_W) = \underbrace{-0.1952}_{C_{7,SM}^{0,\mathrm{eff}}(M_W)} \quad \underbrace{-0.0411}_{\Delta C_{7,SM}^{1}(M_W)} \quad \underbrace{+1.5992}_{C_{7,NP}^{0,\mathrm{eff}}(M_W)} \quad \underbrace{-0.6548}_{\Delta C_{7,NP}^{1}(M_W)} = +0.7081, \tag{91}$$

at the matching scale $\mu_W = M_W$, and

$$C_7^{\mathrm{eff}}(m_b) = \underbrace{-0.3137}_{C_{7,SM}^{0,\mathrm{eff}}(m_b)} \quad \underbrace{+0.0082}_{\Delta C_{7,SM}^{1}(m_b)} \quad \underbrace{+1.2024}_{C_{7,NP}^{0,\mathrm{eff}}(m_b)} \quad \underbrace{-0.3320}_{\Delta C_{7,NP}^{1}(m_b)} = +0.5649, \tag{92}$$

at the lower scale $\mu_b = m_b$. From the numerical values in Eqs. (91) and (92), one can see the following:

(i) In the SM, the NLO QCD contribution $\Delta C_{7,SM}^1(M_W)$ has the same sign with its LO counterpart $C_{7,SM}^{0,\mathrm{eff}}(M_W)$ and is about 12% of $C_{7,SM}^{0,\mathrm{eff}}(M_W)$. After the QCD evolution from M_W to the low energy scale m_b, the NLO QCD part $\Delta C_{7,SM}^1(m_b)$ changed its sign and tended to cancel $C_{7,SM}^{0,\mathrm{eff}}(m_b)$. But the NLO QCD part is now only 2.6% of $C_{7,SM}^{0,\mathrm{eff}}(m_b)$, and practically negligible for $\mu_b \approx m_b$.

(ii) In model III and at the matching scale M_W, the NLO QCD contribution $\Delta C_{7,NP}^1(M_W)$ has the opposite sign of its

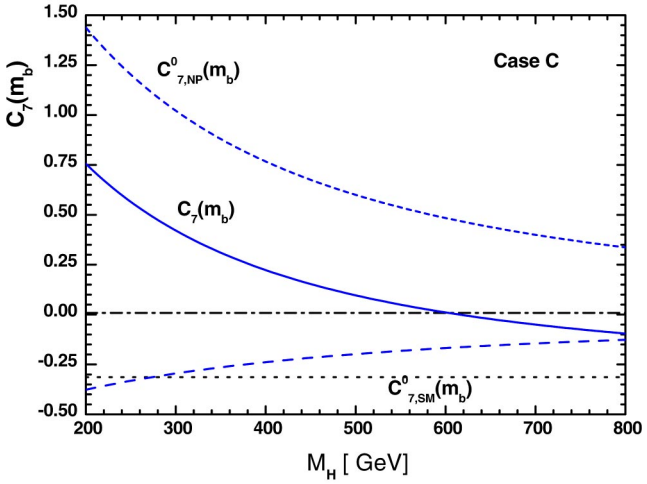

FIG. 11. The M_H dependence of the Wilson coefficient $C_7^{\rm eff}(m_b)$ and its SM and model III parts for $(\lambda_{tt},\lambda_{bb})=(0.5,22)$ (i.e., case C). For details, see text.

LO counterpart and is as large as 41% of $C_{7,NP}^{0,\rm eff}(M_W)$. Unlike the situation in the SM, the NLO new physics contribution to C_7 in model III will cancel its LO counterpart effectively, as shown explicitly in Eq. (91).

(iii) In model III and at the low energy scale m_b, the NLO QCD contribution $\Delta C_{7,NP}^1(m_b)$ and $C_{7,NP}^{0,\rm eff}(m_b)$ still have the opposite sign, but the ratio of these two parts is lowered from 41% to 28%. The NLO and LO parts still cancel effectively.

(iv) Through the QCD running from M_W to m_b, the Wilson coefficient $C_{7,SM}^{\rm eff}$ changed its value from -0.2363 to -0.3055, increasing by about 29% in magnitude. For the new physics part, $C_{7,NP}^{\rm eff}$ decreases by 8%.

The numerical values in Eqs. (91) and (92) are obtained by assuming $M_H=250$ GeV. For different values of M_H, the SM contributions remain unchanged, but the new physics part as well as their sum $C_7^{\rm eff}(m_b)$ will change greatly, as illustrated in Fig. 11. The horizontal dots and dot-dashed line in Fig. 11 correspond to $C_{7,SM}^{0,\rm eff}(m_b)=-0.3137$ and $\Delta C_{7,SM}^{1,\rm eff}(m_b)=0.0082$, respectively. The short-dashed and dashed curve show the new physics contribution $C_{7,NP}^{0,\rm eff}(m_b)$ and $\Delta C_{7,NP}^1(m_b)$, respectively. Finally, the solid curve is the sum of those four parts. Since the dominant part $C_{7,NP}^{0,\rm eff}(m_b)$ decreases rapidly for increasing M_H, the NLO part $\Delta C_{7,NP}^1(m_b)$ changes slowly and the SM parts remain unchanged. The Wilson coefficient $C_7^{\rm eff}(m_b)$ changes rapidly from a large positive value to a small negative value within the range of $200\leqslant M_H\leqslant 800$ GeV as shown by the solid curve in Fig. 11, and will approach the value of its SM counterpart for the heavier charged Higgs boson.

One should note that when $C_7^{\rm eff}(\mu_b)$ becomes small, other previously ''small'' NLO terms $V(\mu_b)$, $A(\mu_b)$, and Δ may play an important rule. The typical numerical values of those terms appeared in the brackets of Eq. (69) and their sum R,

$$R=|\bar{D}|^2+A(m_b)+\Delta, \tag{93}$$

are listed in Table II. In the SM, the relative strength of individual terms are

$$C_7^{\rm eff}(m_b):V(m_b)=1:0.079, \tag{94}$$

$$R:|\bar{D}|^2:A(m_b):\Delta=1:0.98:0.030:(-0.011). \tag{95}$$

The Wilson coefficient $C_7^{\rm eff}(m_b)$ clearly dominates the total contribution in the SM, while the radiative correction $A(m_b)$ and the nonperturbative correction Δ play a minor rule since they are small in size and also cancel each other.

In model III, however, the situation is very different because $C_7^{\rm eff}(m_b)$ and all other terms appeared in the bracket of Eq. (69) will be changed by the inclusion of charged Higgs contributions through the modified Wilson coefficients $C_{7,8}^{0,\rm eff}(m_b)$ and $C_{7,8}^{1,\rm eff}(m_b)$, as can be seen from the numerical results listed in Table II and the curves shown in Fig. 12. The new features are the following:

(1) Along with the increase of M_H, the Wilson coefficient $C_7^{\rm eff}(m_b)$ decreases rapidly, while $V(m_b)$ increases with less speed. Consequently, the ''dominant'' term $|\bar{D}|^2$ decreases more quickly than $C_7^{\rm eff}(m_b)$ and approaches the minimum of $|\bar{D}|^2=0.002$ for $M_H\approx 480$ GeV, which leads to a negative R

TABLE II. The numerical values of the NLO terms appearing in the brackets in Eq. (69) and the branching ratio $\mathcal{B}(B\to X_s\gamma)$ (in units of 10^{-4}) in the SM and the model III of case C, for typical values of mass M_H (in units of GeV). The term R is the summation of the terms $|\bar{D}|^2, A(m_b)$, and Δ.

		$C_7^{\rm eff}(m_b)$	$V(m_b)$	$\lvert\bar{D}\rvert^2$	$A(m_b)$	Δ	R	$\mathcal{B}$
SM		-0.3055	$-0.024-0.015i$	0.1089	0.0033	-0.0012	0.1110	3.52
	200	0.7559	$-0.246+0.043i$	0.2615	0.0138	-0.0513	0.2240	7.10
	250	0.5649	$-0.208+0.036i$	0.1283	0.0092	-0.0333	0.1042	3.30
	300	0.4210	$-0.180+0.024i$	0.0591	0.0064	-0.0222	0.0433	1.37
	400	0.2229	$-0.140+0.020i$	0.0073	0.0037	-0.0102	0.0008	0.03
Model III	600	0.0105	$-0.096+0.009i$	0.0074	0.0023	-0.0022	0.0075	0.24
	800	-0.0951	$-0.074+0.002i$	0.0286	0.0022	-0.0002	0.0305	0.97
	1000	-0.1553	$-0.061-0.002i$	0.0467	0.0023	0.0003	0.0493	1.56
	2000	-0.2580	$-0.037-0.010i$	0.0873	0.0028	-0.0001	0.0900	2.85
	3000	-0.2827	$-0.031-0.012i$	0.0986	0.0031	-0.0006	0.1011	3.21

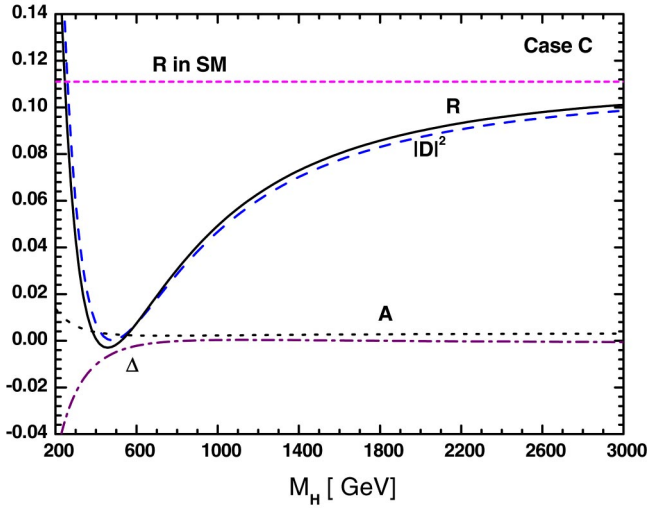

FIG. 12. The M_H dependence of the terms appeared in the brackets of Eq. (69) and the summation R in the SM and model III of case C. For details, see text.

and consequently a negative branching ratio: an unphysical result. For heavier charged Higgs boson, the new physics contributions become smaller and smaller, while the summation of individual terms in the brackets of Eq. (69) restores to its SM value slowly, as illustrated by the solid curve in Fig. 12. For $M_H > 600$ GeV, the terms $A(m_b)$ and Δ remain basically unchanged. As shown in Fig. 7, the new physics contributions approach zero when M_H approaches infinity. This is the so-called decoupling behavior of the Higgs boson.

(2) From Table II and Fig. 12, one can infer that there are two regions of M_H allowed by the measured $\mathcal{B}(B \to X_s\gamma)$. This point can be seen more directly from Fig. 13.

In Fig. 13, we draw the M_H dependence of the branching ratio $\mathcal{B}(B \to X_s\gamma)$ in model III of case C: $(\lambda_{tt}, \lambda_{bb}) = (0.5, 22)$. In both (a) and (b), the band between two dot-dashed horizontal lines shows the data within 2σ errors. The shaded band shows the SM prediction and the error as given in Eq. (79). The dashed and solid curves correspond to the LO and NLO model III predictions, respectively. In order to show the effects of NLO corrections, we use the same values of $(\lambda_{tt}, \lambda_{bb}) = (0.5, 22)$ as input for both LO and NLO theoretical predictions. Figure 13(b) is a magnification of the light Higgs part of Fig. 13(a). For given $\lambda_{tt} = 0.5, \lambda_{bb} = 22$ and $M_H = 250$ GeV, we find numerically

$$\mathcal{B}(B \to X_s\gamma)^{\rm III}_{NLO} = \Bigg[3.48^{+0.18}_{-0.08}(\mu_b) \pm 0.08(\mathcal{B}_{SL})^{+0.42}_{-0.36} \left(\frac{m_c}{m_b}\right)^{+0.52}_{-0.58} (\alpha_s) \pm 0.26(m_t) \pm 0.04\left(\left|\frac{V_{ts}^* V_{tb}}{V_{cb}}\right|^2\right)\Bigg] \times 10^{-4}$$

$$= (3.48 \pm 0.74) \times 10^{-4}, \qquad (96)$$

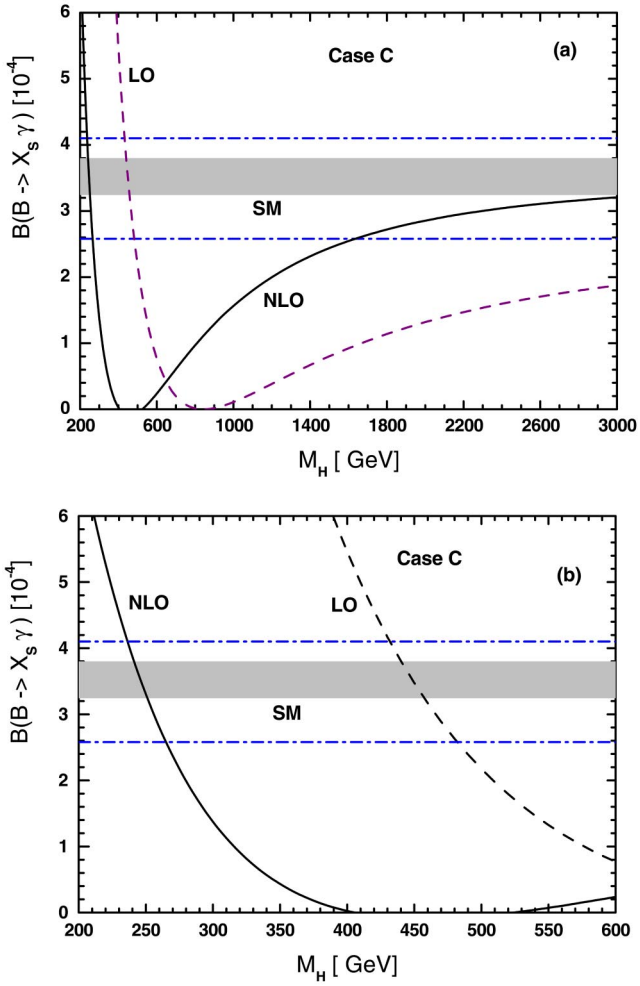

FIG. 13. Plot of the branching ratio vs M_H in model III of case C. The band between two horizontal lines shows the data with 2σ errors, the shaded band shows the SM prediction: $\mathcal{B}(B \to X_s\gamma) = (3.52 \pm 0.28) \times 10^{-4}$. The dashed and solid curves show the LO and NLO model III prediction, respectively. (b) is a magnification of the light Higgs region of (a).

where the central value of the branching ratio is obtained by using the central values of input parameters as given in Appendix A, while the six major errors from the uncertainties of those input parameters are added in quadrature. For asymmetric errors we use the larger value in making quadrature.

For case C, the allowed regions of M_H can be read off from Fig. 13 directly,

$$432 \leqslant M_H \leqslant 478 \ \text{GeV} \qquad (97)$$

at the LO level, and

$$236 \leqslant M_H \leqslant 266 \ \text{GeV} \quad \text{and} \quad M_H \geqslant 1640 \ \text{GeV} \qquad (98)$$

at the NLO level. The first allowed region, a region found interesting by many physicists from the point of view of experimental searches, is shifted to the lower part by about 200 GeV because of the inclusion of NLO contributions.

If we consider the effect of the theoretical error as given in Eq. (96), the limits at the NLO level will become

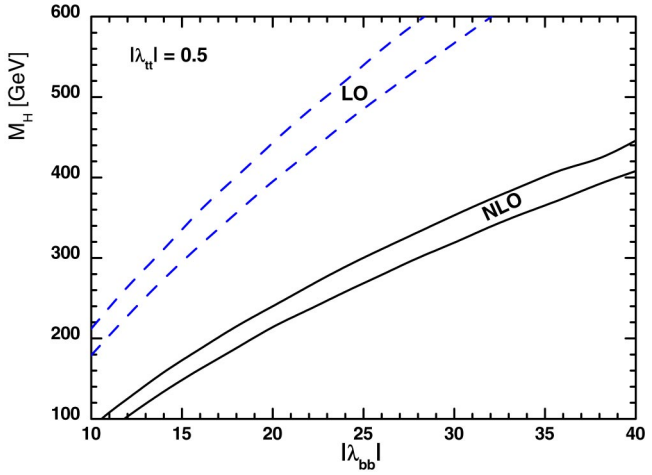

FIG. 14. Contour plot in $|\lambda_{bb}|$-M_H plane obtained by using the LO and NLO model III predictions and the measured decay rate at 2σ level. The regions between two dashed curves and two solid curves are allowed when the LO and NLO theoretical predictions are employed.

$$226 \leqslant M_H \leqslant 285 \text{ GeV} \quad \text{and} \quad M_H \geqslant 1120 \text{ GeV}. \tag{99}$$

The first allowed region has a weak dependence on the theoretical error, but the lower limit of the second allowed region of M_H is very sensitive to the theoretical error.

Figure 14 is the contour plot in $|\lambda_{bb}|$-M_H plane obtained by using the LO and NLO model III predictions and the measured decay rate at 2σ level, while assuming $|\lambda_{tt}| = 0.5$. The regions between two dashed curves and two solid curves are allowed when the LO and NLO theoretical predictions are employed. One can see from Figs. 13 and 14 that a relatively light charged Higgs boson in model III, say around or even less than 200 GeV, is still allowed by the measured branching ratio $\mathcal{B}(B \to X_s\gamma)$. For example, the region

$$188 \leqslant M_H \leqslant 215 \text{ GeV} \tag{100}$$

is allowed by the data if we set $(|\lambda_{tt}|, |\lambda_{bb}|) = (0.5, 18)$ in model III. This is a good news for future experimental searches!

E. Comparison of the results in models II and III

Between the conventional model II and the model III studied here, there is a direct transformation. The results of model III can be reduced to the results of model II by the substitution

$$\lambda_{bb} = -X \to -\tan\beta \quad \text{and} \quad \lambda_{tt} = Y \to 1/\tan\beta. \tag{101}$$

As a comparison, we also present the LO and NLO model II prediction for the branching ratio $\mathcal{B}(B \to X_s\gamma)$ and show the lower limits on M_H obtained from the data. For more details about the rare decay $B \to X_s\gamma$ in model II, one can see, for example, Ref. [4] and references therein.

By using the central values of input parameters as given in Appendix A, and assuming $\tan\beta = 4$, we find the numerical values of the NLO terms appearing in the brackets in Eq. (69) and the branching ratio $\mathcal{B}(B \to X_s\gamma)$ in model II for typical values of M_H, as listed in Table III. In contrast to model III of case C, the differences between the values of the NLO terms in the SM and model II are small and approach zero when M_H approaches infinity. It is easy to see from Table III that the new physics correction to the branching ratio becomes less than 6% and 2% for $M_H = 1000$ and 2000 GeV, respectively.

If we consider the effects of uncertainties of input parameters, we find the branching ratios at the LO and NLO level:

$$\begin{aligned}\mathcal{B}(B \to X_s\gamma)^{\mathrm{II}}_{LO} = \Bigg[& 3.61^{+0.74}_{-0.56}(\mu_b) \pm 0.08(\mathcal{B}_{SL})^{+0.32}_{-0.27}\left(\frac{m_c}{m_b}\right) \\ & \pm 0.09(\alpha_s) \pm 0.08(m_t) \pm 0.04\left(\left|\frac{V^*_{ts}V_{tb}}{V_{cb}}\right|^2\right)\Bigg] \\ & \times 10^{-4} \\ = & (3.61 \pm 0.82) \times 10^{-4} \end{aligned} \tag{102}$$

and

TABLE III. The numerical values of the NLO terms appeared in the brackets in Eq. (69) and the branching ratio $\mathcal{B}(B \to X_s\gamma)$ (in units of 10^{-4}) in model II with $\tan\beta = 4$, for typical values of mass M_H (in units of GeV). The term R is the summation of the terms $|\bar{D}|^2, A(m_b)$, and Δ.

		$C_7^{\mathrm{eff}}(m_b)$	$V(m_b)$	$\lvert\bar{D}\rvert^2$	$A(m_b)$	Δ	R	$\mathcal{B}$
SM		-0.3055	$-0.024-0.015i$	0.1089	0.0033	-0.0012	0.1110	3.52
	200	-0.4034	$-0.004-0.020i$	0.1661	0.0042	-0.0037	0.1666	5.28
	250	-0.3857	$-0.007-0.019i$	0.1547	0.0040	-0.0032	0.1555	4.93
	300	-0.3723	$-0.010-0.019i$	0.1464	0.0039	-0.0028	0.1475	4.68
	400	-0.3540	$-0.014-0.018i$	0.1354	0.0038	-0.0024	0.1368	4.34
Model II	600	-0.3345	$-0.018-0.017i$	0.1242	0.0036	-0.0019	0.1259	3.99
	800	-0.3247	$-0.020-0.016i$	0.1188	0.0035	-0.0017	0.1207	3.83
	1000	-0.3192	$-0.021-0.016i$	0.1158	0.0035	-0.0015	0.1178	3.74
	2000	-0.3098	$-0.023-0.015i$	0.1109	0.0034	-0.0013	0.1131	3.59
	3000	-0.3075	$-0.024-0.015i$	0.1098	0.0034	-0.0012	0.1120	3.55

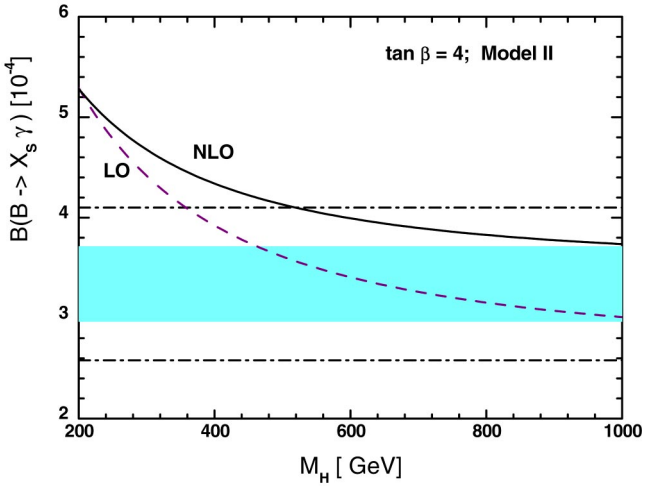

FIG. 15. Plots of the branching ratio $\mathcal{B}(B\to X_s\gamma)$ vs the mass M_H in model II for $\tan\beta=4$. For details see text.

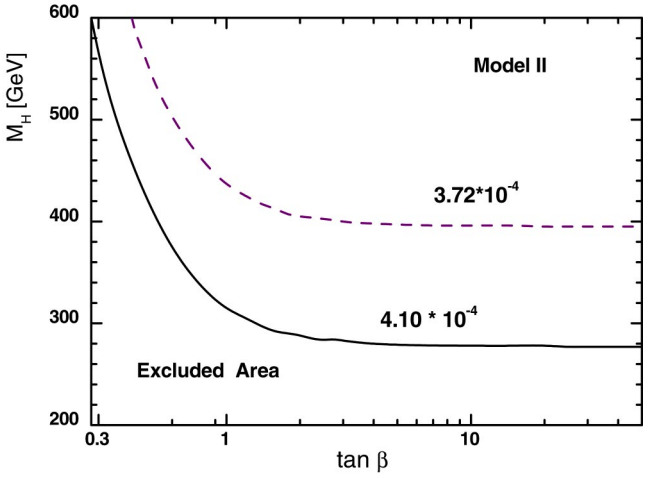

FIG. 16. Contour plot in $\tan\beta$-M_H plane obtained by using the NLO model II predictions and the measured decay rate at 1σ (dashed curve) and 2σ level (solid curve). The excluded region is below the corresponding curves.

$$\mathcal{B}(B\to X_s\gamma)^{\rm II}_{NLO}=\Bigg[4.13^{+0.03}_{-0.17}(\mu_b)\pm 0.09(\mathcal{B}_{SL})^{+0.24}_{-0.20}\left(\frac{m_c}{m_b}\right)$$
$$\pm 0.09(\alpha_s)\pm 0.08(m_t)\pm 0.04\left(\left|\frac{V_{ts}^*V_{tb}}{V_{cb}}\right|^2\right)\Bigg]$$
$$\times 10^{-4}$$
$$=(4.13\pm 0.34)\times 10^{-4}, \tag{103}$$

where the central value is obtained for $M_H=500$ GeV, and the errors connected with the uncertainties of six input parameters are added in quadrature.

Figure 15 shows the M_H dependence of the branching ratio $\mathcal{B}(B\to X_s\gamma)$ in model II at LO and NLO level, assuming $\tan\beta=4$. The shaded band and the band between two horizontal dot-dashed lines show the measured branching ratio $\mathcal{B}(B\to X_s\gamma)$ within 1σ and 2σ errors, respectively. The dashed and solid curves shows the LO and NLO model II prediction. By comparing the theoretical predictions and the measured branching ratios at the 2σ level, it is easy to read off the lower limit on M_H directly from Fig. 15:

$$M_H\geqslant 357\ \text{GeV} \tag{104}$$

at the LO level, and

$$M_H\geqslant 520\ \text{GeV} \tag{105}$$

at the NLO level, if the uncertainties of the input parameters are not taken into account. If we consider the combined uncertainties as given in Eqs. (102) and (103) the lower limit will be changed to

$$M_H\geqslant 298 \quad \text{or} \quad 350\ \text{GeV} \tag{106}$$

at the LO and NLO level, respectively.

Figure 16 is the contour plot in the $\tan\beta$-M_H plane obtained by finding the minimum of the NLO model II prediction of the branching ratio $\mathcal{B}(B\to X_s\gamma)$, when varying the input parameters within their errors and the lower scale μ_b in the range of $2.4\leqslant\mu_b\leqslant 9.6$ GeV, but fixing $\mu_W=M_W$. The excluded region is below the corresponding curves when the measured branching ratio at 1σ (dashed curve) and 2σ level (solid curve) is employed. For $\mathcal{B}(B\to X_s\gamma)\leqslant 4.1\times 10^{-4}$ and $\tan\beta=1,10,20$, the lower limit on M_H is 315, 278, and 277 GeV, respectively. Because of the flatness of the curves shown in Fig. 16 towards the higher end of M_H, the lower limits on M_H are very sensitive to the ways to deal with theoretical errors or the details of the calculations. The lower limit on M_H as illustrated in Fig. 16 is consistent with that given in Ref. [4].

The major differences between model II and model III studied here and the causes inducing such differences are the following:

(1) In model II, the region of $\tan\beta\leqslant 1$ is strongly disfavored by the measured ΔM_{B_d} and other experimental terms. In the region $\tan\beta\geqslant 4$, we have $|Y|^2=1/\tan^2\beta\ll 1$ and $XY^*\equiv 1$. The possible new physics contributions to the Wilson coefficients $C_{7,8}$ are small in magnitude and have the same sign as their SM counterparts and therefore are strongly constrained by the excellent agreement between the data and the SM prediction for $B\to X_s\gamma$ decay.

(2) In model III, the new physics contributions proportional to $|\lambda_{tt}|^2$ and $|\lambda_{tt}||\lambda_{bb}|$ have the opposite sign for $\theta=0°$ and will cancel each other. Even if $|\lambda_{tt}|$ should be smaller than 1 due to the strong constraint from the measured mass difference ΔM_{B_d} as discussed in preceding section, the inclusion of the new physics contribution still can change the sign of the Wilson coefficient $C_7^{\rm eff}(m_b)$ from negative in the SM to positive in model III. On the experimental side, current data still cannot exclude the possibility of a positive Wilson coefficient $C_7^{\rm eff}(m_b)$.

(3) Other NLO terms in the bracket of Eq. (69) also receive new physics corrections, and therefore the cancellation between individual terms in model III is very different from the pattern in model II.

(4) The inclusion of NLO contributions will decrease the lower limit on M_H in model III. In model II, in contrast, the

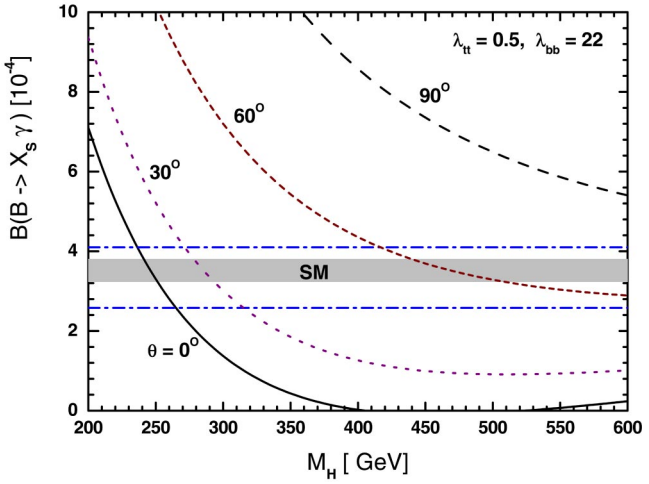

FIG. 17. Plots of the branching ratio $\mathcal{B}(B\to X_s\gamma)$ vs the mass M_H in model III for case C and for θ=0° (solid curve), 30° (dots curve), 60° (short-dashed curve), and 90° (dashed curve), respectively. The band between two horizontal dot-dashed lines shows the measured branching ratio within 2σ errors.

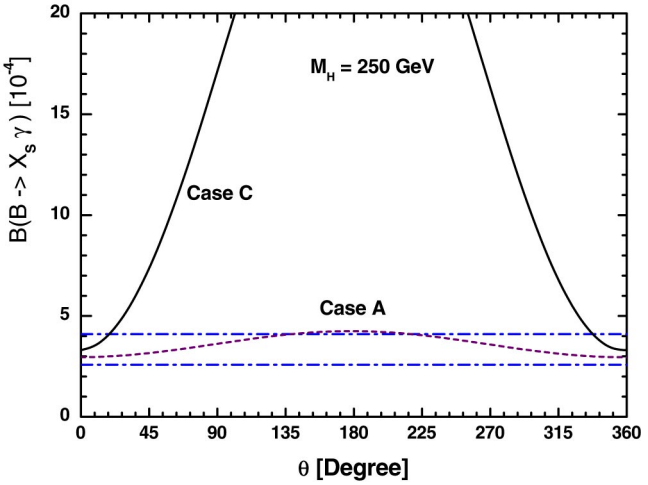

FIG. 18. Plots of the branching ratio $\mathcal{B}(B\to X_s\gamma)$ vs the phase θ in model III for case A (short-dashed curve) and case C (solid curve), and assuming M_H=250 GeV. The band between two horizontal dot-dashed lines shows the measured branching ratio within 2σ errors.

lower limit will go up by including the NLO corrections.

(5) In the model III studied here, a light charged Higgs boson with a mass around or even less than 200 GeV is still allowed at the NLO level. In model II, however, such a light charged Higgs boson seems impossible.

F. Effects of a nonzero phase θ

For the mass splitting ΔM_{B_d}, the new physics contributions in model III depend on $|\lambda_{tt}|^2$ and $|\lambda_{tt}|^4$, and therefore are independent of the phase of coupling λ_{tt}. For the $B\to X_s\gamma$ decay, however, the dominant new physics contributions [i.e., the third terms in Wilson coefficients $C_{7,8}^{0,\mathrm{eff}}(M_W)$ and $C_{7,8}^{1,\mathrm{eff}}(M_W)$ in Eqs. (45), (46) and (56), (57)] depend on the relative phase θ between λ_{tt} and λ_{bb}, as can be seen from Eq. (62). In previous calculations, we always assume θ=0°. Here we will consider the effect of a nonzero phase θ.

Figure 17 shows the M_H dependence of the branching ratio $\mathcal{B}(B\to X_s\gamma)$ in model III for case C [i.e., $(|\lambda_{tt}|,|\lambda_{tt}|)=(0.5,22)$] and for θ=0° (solid curve), 30° (dots curve), 60° (short-dashed curve), and 90° (dashed curve), respectively. The band between two horizontal dot-dashed lines shows the measured branching ratio within 2σ errors. The shaded area shows the SM prediction with the error as given in Eq. (79). It is easy to see from Fig. 17 that the nonzero phase will strengthen the constraint on the mass M_H in case C. For θ=30°, the allowed region is shifted to

$$271\leqslant M_H\leqslant 317\ \mathrm{GeV}. \tag{107}$$

For θ=60°, the lower limit on M_H goes up to 417 GeV. For $\theta\geqslant$75°, the lower limit on M_H is higher than 600 GeV.

In Fig. 18, we show the θ dependence of the branching ratio $\mathcal{B}(B\to X_s\gamma)$ in model III for case A (the short-dashed curve) and case C (the solid curve) discussed in previous subsections, and for given M_H=250 GeV. Obviously, only two narrow regions of θ, $0°\lesssim\theta\lesssim 20°$ and $340°\lesssim\theta\lesssim 360°$, are allowed by the data for case C. For case A, however, almost the whole ranges of θ are still allowed by the data of the $B\to X_s\gamma$ decay.

V. SUMMARY

In this paper, we calculated the new physics contributions to the mass splitting ΔM_{B_d} and the branching ratio $\mathcal{B}(B\to X_s\gamma)$ induced by the charged Higgs loop diagrams in model III, and found the constraints on the parameters of model III by comparing the theoretical predictions with the high precision data. We focus on the effects of the NLO QCD corrections on these two physical observables.

In Sec. II, we gave a brief review about the structure of the general two-Higgs-doublet models and the phenomenological studies about such models. Following previous works [18], we assume that only the diagonal Yukawa couplings λ_{tt} and λ_{bb} are nonzero for the model III under consideration in this paper and study the effects of NLO new physics contributions.

In Sec. III, we calculated the new physics contributions to the mass splitting ΔM_{B_d} in model III at the NLO level. The magnitude of the Yukawa coupling λ_{tt} is strongly constrained by the precision data $\Delta M_{B_d}=0.502\pm 0.007\ \mathrm{ps}^{-1}$. As shown in Figs. 4 and 5, the upper limit on λ_{tt} is $|\lambda_{tt}|\leqslant 1.7$, while the choice of $|\lambda_{tt}|\approx 0.5$ is favored by the measured ΔM_{B_d} if one requires the charged Higgs boson to be light, say around 200 GeV.

In Sec. IV, we calculated the new physics contributions to the rare decay $B\to X_s\gamma$ in model III. The NLO QCD corrections are taken into account here. The new physics contributions to the Wilson coefficients $C_{7,8}^{0,1}(\mu)$ and the interference between the new physics parts and their SM counterparts are investigated. The new physics contributions to the $B\to X_s\gamma$ decay and possible constraints on $|\lambda_{bb}|$ and M_H are calculated and analyzed. Three typical cases for the choice of Yukawa couplings $|\lambda_{tt}|$ and $|\lambda_{bb}|$ are studied in great detail.

The common features and the differences between the conventional model II and model III, as well as the effects of a nonzero relative phase θ, are also considered. From the numerical results, we found the following:

(a) In the model III studied here, a light charged Higgs boson with a mass around or even less than 200 GeV is still allowed at the NLO level by the measured branching ratio $\mathcal{B}(B\to X_s\gamma)$ within 2σ errors, as can be seen in Eq. (100) and Figs. 13 and 14. In model II, however, such a light charged Higgs boson seems impossible.

(b) The inclusion of the NLO QCD contributions will decrease the lower limit on M_H by about 200 GeV in model III. In model II, in contrast, the lower limit on M_H will be increased by about 160 GeV because of the inclusion of the NLO corrections.

(c) As illustrated in Fig. 17, the allowed region of M_H in model III will be shifted toward the heavy mass end for a nonzero relative phase θ.

ACKNOWLEDGMENTS

Z.J.X is very grateful to the high energy section of ICTP, Italy, where part of this work was done, for warm hospitality and financial support. This work was supported by the National Natural Science Foundation of China under Grant Nos. 10075013 and 10275035, and by the Research Foundation of Nanjing Normal University under Grant No. 214080A916.

APPENDIX A: INPUT PARAMETERS AND RUNNING COUPLINGS

In this appendix we list the input parameters used in our calculations. The values of most parameters are quoted from Refs. [2,3] directly. The masses m_t, m_b, m_c are understood to be the pole mass, while $\overline{m}_q(\mu)$ is the running q-quark mass in the modified minimal subtraction ($\overline{\rm MS}$) scheme at the renormalization scale μ. To first order in α_S, the running mass $\overline{m}_q(\mu)$ and the pole mass m_q are related through [4]

$$\overline{m}_q(\mu)=m_q\left[1+\frac{\alpha_S(\mu)}{\pi}\left(\ln\frac{m_q^2}{\mu^2}-\frac{4}{3}\right)\right]. \tag{A1}$$

The masses, coupling constants, and other input parameters are [2,3]

$$\begin{gathered} M_{B_d}=5.279\ \text{GeV},\quad m_b=4.8\pm0.2\ \text{GeV},\\ m_c/m_b=0.29\pm0.02;\\ M_W=80.42\ \text{GeV},\quad m_t=174.3\pm5.1\ \text{GeV},\\ \alpha_S(M_Z)=0.119\pm0.004,\quad \alpha_{em}=1/137.056,\\ \lambda_1=-0.50\ \text{GeV}^2,\quad \lambda_2=0.12\ \text{GeV}^2. \end{gathered} \tag{A2}$$

The ratio of CKM elements $|V_{ts}^*V_{tb}/V_{cb}|^2$ appearing in the decay rate $\mathcal{B}(B\to X_s\gamma)$ can be expressed in terms of the Wolfenstein parameters as follows:

$$\begin{aligned}\left|\frac{V_{ts}^*V_{tb}}{V_{cb}}\right|^2&=1-\lambda^2(1-2\bar{\rho})+\lambda^4(\bar{\rho}^2+\bar{\eta}^2-A^2)+\mathcal{O}(\lambda^6)\\&=0.971\pm0.010,\end{aligned} \tag{A3}$$

where we have used $\lambda=0.2196$, $A=0.854$, $\bar{\rho}=0.22\pm0.10$, and $\bar{\eta}=0.35\pm0.05$ [2]. The error induced by $\delta\bar{\eta}=0.05$ is only 0.0001 for the ratio.

For the semileptonic branching ratio $\mathcal{B}_{SL}=\mathcal{B}(B\to X_c e\bar{\nu}_e)$ we use

$$\mathcal{B}_{SL}=(10.64\pm0.23)\%, \tag{A4}$$

as given in Ref. [2].

Finally, for the running of $\alpha_s(\mu)$, we use the two-loop formulas as given in Ref. [40]:

$$\alpha_s=\frac{\alpha_s(M_Z)}{v(\mu)}\left[1-\frac{\beta_1}{\beta_0}\frac{\alpha_s(M_Z)}{4\pi}\frac{\ln[v(\mu)]}{v(\mu)}\right], \tag{A5}$$

with

$$v(\mu)=1-\beta_0\frac{\alpha_s(M_Z)}{2\pi}\ln\left(\frac{M_Z}{\mu}\right), \tag{A6}$$

where $\beta_0=23/3$ and $\beta_1=116/3$ for b quark decays.

APPENDIX B: NLO WILSON COEFFICIENTS AT $\mu=M_W$

For the completeness, we list here the NLO functions at the matching scale μ_W appearing in Eqs. (54), (56), and (57). For more details see Ref. [4]. In the SM, we have

$$E_0(x)=\frac{x(x^2+11x-18)}{12(x-1)^3}+\frac{x^2(4x^2-16x+15)}{6(x-1)^4}\ln x-\frac{2}{3}\ln x-\frac{2}{3}, \tag{B1}$$

$$\begin{aligned}W_{7,SM}(x)=&\frac{-16x^4-122x^3+80x^2-8x}{9(x-1)^4}\mathrm{Li}_2\left(1-\frac{1}{x}\right)+\frac{6x^4+46x^3-28x^2}{3(x-1)^5}\ln^2x\\&+\frac{-102x^5-588x^4-2262x^3+3244x^2-1364x+208}{81(x-1)^5}\ln x\\&+\frac{1646x^4+12205x^3-10740x^2+2509x-436}{486(x-1)^4},\end{aligned} \tag{B2}$$

$$W_{8,SM}(x)=\frac{-4x^4+40x^3+41x^2+x}{6(x-1)^4}\mathrm{Li}_2\left(1-\frac{1}{x}\right)+\frac{-17x^3-31x^2}{2(x-1)^5}\ln^2 x$$
$$+\frac{-210x^5+1086x^4+4893x^3+2857x^2-1994x+280}{216(x-1)^5}\ln x$$
$$+\frac{737x^4-14102x^3-28209x^2+610x-508}{1296(x-1)^4}, \tag{B3}$$

$$T_{7,SM}(x)=\frac{x}{3}\left[\frac{47x^3-63x^2+9x+7-(18x^3+30x^2-24x)\ln x}{(x-1)^5}\right], \tag{B4}$$

$$T_{8,SM}(x)=2x\left[\frac{-x^3-9x^2+9x+1+(6x^2+6x)\ln x}{(x-1)^5}\right], \tag{B5}$$

where $x=m_t^2/M_W^2$.

In the 2HDMs, the NLO functions describing the charged Higgs contributions are

$$E_H(y)=\frac{y}{36}\left[\frac{7y^3-36y^2+45y-16+(18y-12)\ln y}{(y-1)^4}\right], \tag{B6}$$

$$W_{7,YY}(y)=\frac{2y}{9}\left[\frac{8y^3-37y^2+18y}{(y-1)^4}\mathrm{Li}_2\left(1-\frac{1}{y}\right)+\frac{3y^3+23y^2-14y}{(y-1)^5}\ln^2 y+\frac{21y^4-192y^3-174y^2+251y-50}{9(y-1)^5}\ln y\right.$$
$$\left.+\frac{-1202y^3+7569y^2-5436y+797}{108(y-1)^4}\right]-\frac{4}{9}E_H, \tag{B7}$$

$$W_{8,YY}(y)=\frac{y}{6}\left[\frac{13y^3-17y^2+30y}{(y-1)^4}\mathrm{Li}_2\left(1-\frac{1}{y}\right)-\frac{17y^2+31y}{(y-1)^5}\ln^2 y+\frac{42y^4+318y^3+1353y^2+817y-226}{36(y-1)^5}\ln y\right.$$
$$\left.+\frac{-4451y^3+7650y^2-18153y+1130}{216(y-1)^4}\right]-\frac{1}{6}E_H, \tag{B8}$$

$$M_{7,YY}(y)=\frac{y}{27}\left[\frac{-14y^4+149y^3-153y^2-13y+31-(18y^3+138y^2-84y)\ln y}{(y-1)^5}\right], \tag{B9}$$

$$M_{8,YY}(y)=\frac{y}{36}\left[\frac{-7y^4+25y^3-279y^2+223y+38+(102y^2+186y)\ln y}{(y-1)^5}\right], \tag{B10}$$

$$T_{7,YY}(y)=\frac{1}{3}T_{7,SM}(x\to y), \tag{B11}$$

$$T_{8,YY}(y)=\frac{1}{3}T_{8,SM}(x\to y), \tag{B12}$$

and

$$W_{7,XY}(y)=\frac{4y}{3}\left[\frac{8y^2-28y+12}{3(y-1)^3}\mathrm{Li}_2\left(1-\frac{1}{y}\right)+\frac{3y^2+14y-8}{3(y-1)^4}\ln^2 y+\frac{4y^3-24y^2+2y+6}{3(y-1)^4}\ln y+\frac{-2y^2+13y-7}{(y-1)^3}\right], \tag{B13}$$

$$W_{8,XY}(y) = \frac{y}{3}\left[\frac{17y^2-25y+36}{2(y-1)^3}\mathrm{Li}_2\left(1-\frac{1}{y}\right) - \frac{17y+19}{(y-1)^4}\ln^2 y + \frac{14y^3-12y^2+187y+3}{4(y-1)^4}\ln y - \frac{3(29y^2-44y+143)}{8(y-1)^3}\right], \tag{B14}$$

$$M_{7,XY}(y) = \frac{2y}{9}\left[\frac{-8y^3+55y^2-68y+21-(6y^2+28y-16)\ln y}{(y-1)^4}\right], \tag{B15}$$

$$M_{8,XY}(y) = \frac{y}{6}\left[\frac{-7y^3+23y^2-97y+81+(34y+38)\ln y}{(y-1)^4}\right], \tag{B16}$$

$$T_{7,XY}(y) = \frac{2y}{3}\left[\frac{13y^2-20y+7-(6y^2+4y-4)\ln y}{(y-1)^4}\right], \tag{B17}$$

$$T_{8,XY} = 2y\left[\frac{-y^2-4y+5+(4y+2)\ln y}{(y-1)^4}\right]. \tag{B18}$$

where $y = m_t^2/M_H^2$.

[1] C. Jessop, SLAC Publication No. 9610.

[2] Particle Data Group, K. Hagiwara *et al.*, Phys. Rev. D **66**, 010001 (2002) and 2003 partial update for edition 2004 (URL: http://pdg.lbl.gov).

[3] LEP B oscillation Working Group, http://www.cern.ch/LEPBOSC/

[4] F.M. Borzumati and C. Greub, Phys. Rev. D **58**, 074004 (1998); **59**, 057501 (1999) (Addendum).

[5] J. Urban, F. Krauss, U. Jentschura, and G. Soff, Nucl. Phys. **B523**, 40 (1998).

[6] K.G. Chetyrkin, M. Misiak, and M. Munz, Phys. Lett. B **400**, 206 (1997); **425**, 414(E) (1998).

[7] A.L. Kagan and M. Neubert, Eur. Phys. J. C **7**, 5 (1999).

[8] A.J. Buras, A. Czarnecki, M. Misiak, and J. Urban, Nucl. Phys. **B611**, 488 (2001); **B631**, 219 (2002), and reference therein.

[9] P. Gambino and M. Misiak, Nucl. Phys. **B611**, 338 (2001).

[10] For a recent review see T. Hurth, hep-ph/0212304.

[11] For recent developments see C. Greub, talk presented at the EPS-2003, 2003, Aachen, Germany.

[12] M. Ciuchini, G. Degrassi, P. Gambino, and G.F. Giudice, Nucl. Phys. **B527**, 21 (1998).

[13] P. Ciafaloni, A. Romanino, and A. Strumia, Nucl. Phys. **B524**, 361 (1998).

[14] M. Ciuchini, G. Degrassi, P. Gambino, and G.F. Giudice, Nucl. Phys. **B534**, 3 (1998); G. Degrassi, P. Gambino, and G.F. Ciudice, J. High Energy Phys. **12**, 009 (2000).

[15] C. Bobeth, M. Misiak, and J. Urban, Nucl. Phys. **B567**, 567 (2000).

[16] D. Atwood, L. Reina, and A. Soni, Phys. Rev. D **54**, 3296 (1996).

[17] D. Atwood, L. Reina, and A. Soni, Phys. Rev. D **55**, 3156 (1997).

[18] D.B. Chao, K. Cheung, and W.Y. Keung, Phys. Rev. D **59**, 115006 (1999).

[19] Z.J. Xiao, C.S. Li, and K.T. Chao, Phys. Lett. B **473**, 148 (2000); Phys. Rev. D **62**, 094008 (2000).

[20] K. Kiers, A. Soni, and G.H. Wu, Phys. Rev. D **59**, 096001 (1999); **62**, 116004 (2000); G.H. Wu and A. Soni, *ibid.* **62**, 056005 (2000).

[21] C.D. Lü and Z.J. Xiao, Phys. Rev. D **53**, 2529 (1996).

[22] T.P. Cheng and M. Sher, Phys. Rev. D **35**, 3484 (1987); M. Sher and Y. Yuan, *ibid.* **44**, 1461 (1991); W.S. Hou, Phys. Lett. B **296**, 179 (1992); A. Antaramian, L.J. Hall, and A. Rasin, Phys. Rev. Lett. **69**, 1871 (1992); L.J. Hall and S. Winberg, Phys. Rev. D **48**, R979 (1993); D. Chang, W.S. Hou, and W.Y. Keung, *ibid.* **48**, 217 (1993); Y.L. Wu and L. Wolfenstein, Phys. Rev. Lett. **73**, 1762 (1994); D. Atwood, L. Reina, and A. Soni, *ibid.* **75**, 3800 (1995).

[23] S. Glashow and S. Weinberg, Phys. Rev. D **15**, 1958 (1977).

[24] J.F. Gunion, H.E. Haber, G. Kane, and S. Dawson, *The Higgs Hunter's Guide* (Addison Wesley, Redwood City, 1990), and references therein.

[25] M. Kabayashi, T. Maskawa, Prog. Theor. Phys. **49**, 652 (1973).

[26] W.S. Hou and R.S. Willey, Phys. Lett. B **202**, 59 (1988); S. Bertolini *et al.*, Nucl. Phys. **B353**, 591 (1991); C.D. Lü, *ibid.* **B441**, 33 (1994).

[27] P. Gambino, J. Phys. G **27**, 1199 (2001).

[28] T.M. Aliev and E.O. Iltan, J. Phys. G **25**, 989 (1999).

[29] Z.J. Xiao, C.S. Li, and K.T. Chao, Phys. Rev. D **63**, 074005 (2001); J.J. Cao, Z.J. Xiao, and G.R. Lu, *ibid.* **64**, 014012 (2001); D. Zhang, Z.J. Xiao, and C.S. Li, *ibid.* **64**, 014014 (2001); Z.J. Xiao, K.T. Chao, and C.S. Li, *ibid.* **65**, 114021 (2002).

[30] L.F. Abbot, P. Sikivie, and M.B. Wise, Phys. Rev. D **21**, 1393 (1980); S.L. Glashow and E.E. Jenkins, Phys. Lett. B **196**, 233 (1987); G.G. Athanasiu, P.J. Franzini, and F.J. Gilman, Phys. Rev. D **32**, 3010 (1985); C.Q. Geng and J.N. Ng, *ibid.* **32**, 3010 (1985).

[31] A.J. Buras, M. Jamin, and P.H. Weisz, Nucl. Phys. **B347**, 491 (1990).

[32] A. Grant, Phys. Rev. D **51**, 207 (1995).

[33] M. Battaglia *et al.*, in Proceedings of the First Workshop on the CKM Unitarity Triangle, CERN 2002, hep-ph/0304132.

[34] G. Buchalla, A.J. Buras, and M.E. Lautenbacher, Rev. Mod. Phys. **68**, 1125 (1996).
[35] A. Czarnecki and W.J. Marciano, Phys. Rev. Lett. **81**, 277 (1998).
[36] N. Cabibbo and L. Maiani, Phys. Lett. **79B**, 109 (1978); Y. Nir, Phys. Lett. B **221**, 184 (1989).
[37] A. Ali and C. Greub, Z. Phys. C **49**, 431 (1991); Phys. Lett. B **259**, 182 (1991); **361**, 146 (1995); N. Pott, Phys. Rev. D **54**, 938 (1996).
[38] A. Falk, M. Luke, and M. Savage, Phys. Rev. D **49**, 3367 (1994).
[39] M.B. Voloshin, Phys. Lett. B **397**, 275 (1997); Z. Ligeti, L. Randall, and M.B. Wise, *ibid.* **402**, 178 (1997); A.K. Grant, A.G. Morgan, S. Nussinov , and R.D. Peccei, Phys. Rev. D **56**, 3151 (1997); G. Buchalla, G. Isidori, and S.J. Rey, Nucl. Phys. **B511**, 594 (1998).
[40] A.J. Buras, in *Probing the Standard Model in Particle Interactions*, edited by F. Davia and R. Gupta (Elsevier Science B.V., Amsterdam, 1998).